DISSERTATION IN PHYSICS

NEUTRON SCATTERING STUDY ON SOFT PHONON MODES IN $CsPbCl_3$

Yasuhiko FUJII

THE OSAKA UNIVERSITY

GRADUATE SCHOOL OF SCIENCE

TOYONAKA, OSAKA

Neutron Scattering Study on Soft Phonon Modes in $CsPbCl_3$

Yasuhiko FUJII

May 1973

Contents

Synopsis

Neutron scattering experiments were carried out in order to investigate the mechanism of the successive phase transitions in $CsPbCl_3$. Perovskite crystal $CsPbCl_3$ undergoes three successive phase transitions at T=47°C, 42°C and 37°C. It has been elucidated that these phase transitions are basically associated with the condensation of rotational modes of $PbCl_6$ octahedra around the three principal axes.

(1) The phase transition at 47°C is caused by the condensation of the non-degenerate M_3 phonon mode at the zone boundary along the [110] direction of the cubic lattice. The axis of rotation of the $PbCl_6$ octahedra is along the [001] axis.

(2) The phase transition at 42°C is associated with the condensation of one of doubly degenerate modes Z_5^x and Z_5^y at the zone boundary along the $[001]_t$ direction of the tetragonal lattice which are derived from the triply degenerate R_{25} mode in the cubic phase. The direction of the rotation axis is along the [100] when we assign Z_5^x as the condensing mode.

(3) The phase transition at 37°C is caused by the condensation of the remaining Z_5^y mode.

(4) Both the M_3 and R_{25} modes are overdamped in the cubic phase even at 80°C.

The crystal system and space groups at each phase determined from the eigen vectors of the condensing modes are;

Phase II (42°C<T<47°C) tetragonal D_{4h}^5- P4/mbm,

Phase III(37°C<T<42°C)	orthorhombic	D_{2h}^{17}- Cmcm,
Phase IV (T<37°C)	monoclinic	C_{2h}^{2}- $P2_1/m$.

These are consistent with the experimental results on the NQR spectra of Cl^- ion.

A phenomenological theory to explain these successive phase transitions caused by the condensation of the M_3 and R_{25} zone boundary phonons was developed. It is shown that by a suitable choice of the parameters included in the expansion of the free energy up to the sixth order with respect to rotation angles, the observed phase transition schemes can be qualitatively explained.

§1. Introduction

In recent years, extensive investigations have been made on many structural phase transitions, in particular, of the cubic perovskite crystals(Fig.1). Many cubic perovskite crystals undergo phase transitions in which they transform to slightly distorted structures from original perovskites. It is well known that these phase transitions are caused by the condensation of normal modes of the phonon whose eigen vectors correspond to the atomic shifts in the structure stabilized below the transition temperature T_C. The frequency of this phonon mode decreases as the temperature is lowered to T_C, and at T_C the restoring force for this mode vanishes so that the atoms shift to new equiliblium positions. The condensation of the "soft phonon" is very useful concept to understand various structural phase transitions.

In some perovskites such as $BaTiO_3$[1], $PbTiO_3$[2] and $KTaO_3$[3], the transverse optical mode at the zone center softens, which explains the occurrence of ferroelectric phase transitions. Among these, $BaTiO_3$ undergoes three successive phase transitions at 130°C, 5°C and -80°C.[4] The symmetry of this crystal changes as cubic → tetragonal → orthorhombic → rhombohedral as the temperature is lowered. The direction of the spontaneous polarization referred to the cubic lattice is along the [100] in the tetragonal phase, [110] in the orthorhombic phase and [111] in the rhombohedral phase.*) It has been known that these phase transitions were understood in terms of the successive condensations of each of the triply degenerate zone center modes with eigen vectors along the <100> directions.

On the other hand, the phase transitions of $SrTiO_3$ (T_C= 110°K)[5] and $LaAlO_3$ (T_C=535°C)[6] are explained by the softening of the zone boundary mode which is associated with a rotation of BX_6 octahedra around the principal axes of the cubic lattice. This mode belongs to the irreducible representation R_{25} of the cubic point group m3m. However, the structure stabilized by the condensation of the R_{25} mode is somewhat different for these substances: $SrTiO_3$ has a tetragonal symmetry while $LaAlO_3$ has a rhombohedral one. This difference also arises from the degeneracy of the R_{25} mode. Because of the cubic symmetry, R_{25} is triply degenerate. Let us designate each of these three modes as R_{25}^x, R_{25}^y and R_{25}^z where the superscript symbols specify the axes of rotation of the BX_6 octahedra. In $SrTiO_3$, the R_{25}^x mode condenses while in $LaAlO_3$ the condensing mode is given by the linear combination of $R_{25}^x + R_{25}^y + R_{25}^z$(Fig.2). The anharmonicity of the lattice potential determines which one of the arbitrary linear combinations condenses below T_C.[7,8]

In some other perovskites such as $KMnF_3$[9-11] and $NaNbO_3$[12], successive phase transitions associated with the rotational mode have been observed. $KMnF_3$ undergoes the structural phase transitions at 184°K and 92°K. The transition at 184°K is exactly the same as that of $SrTiO_3$[13], while the transition at 92°K

---

*) The notations of crystallographic indices, such as [100] for the crystal axis, (100) for the crystal plane, Laue index 100, reciprocal lattice point $\frac{3}{2},\frac{3}{2},\frac{1}{2}$ and so on, are, hereafter, referred to the cubic lattice in the Phase I, unless otherwise specified by the subscript, such as $[100]_t$.

is caused by the condensation of the M_3 mode at the zone boundary along the [110] direction. This mode also corresponds to the rotation of the BX_6 octahedra. The only difference between the R_{25} and the M_3 is that the R_{25} represents the opposite rotation of the neighboring BX_6 octahedra along the rotation axis, whereas the M_3 represents the rotation in the same direction as illustrated in Fig.3. In the case of $NaNbO_3$, it has been reported that the phase transitions at 640°C and 572°C are caused by the condensation of the M_3 and R_{25} modes, respectively. This is in contrast with the case of $KMnF_3$ in which the R_{25} mode first condenses.

Recently, one of perovskite crystals $CsPbCl_3$ was found to undergo three successive phase transitions. In 1959, Møller[14] first observed the phase transition at 47°C. He also carried out the structure analysis and reported that the basic structure of this crystal was of perovskite type. In 1969, three groups independently found the other transitions. Sakudo et al.[15] observed a broad elastic anomaly near about 40°C. They also found that superlattice reflections in x-ray diffraction pattern appear at the X-point(see Fig.1) at room temperature. Hirotsu and Sawada[16] made optical measurements and confirmed three phase transitions at 37°C, 42°C and 47°C. According to their optical data, the crystal is uniaxial between 47°C and 42°C. Between 42°C and 37°C, the optical elasticity axes in the basal plane are lying along the pseudo-cubic <100> directions. At 37°C, the axes suddenly rotate by 45° pointing along the <110> directions. Hirotsu inferred that the crystal symmetry may transform as cubic → tetragonal → orthorhombic → orthorhombic or monoclinic

when the temperature is lowered. Jensen[17] carried out the NQR measurements on Cl^- ion using powder specimen and obtained interesting results which are depicted in Fig.4. This figure shows three phase transitions in which the transition at 42°C is of the second order and the others are of the first order, and the change of the site symmetry of the Cl^- ions. It is interesting that in the lowest temperature phase, the Cl site seems to restore a higher symmetry. In 1969, studies of the EPR of Mn^{2+} doped in $CsPbCl_3$ was made by Cape et al.[18] They discussed the space groups of the crystal at each phase. In 1970 and 1971, Hirotsu made extensive experimental studies including dielectric, elastic, specific heat, optical and Raman scattering measurements.[19,20] He confirmed that this crystal was not ferroelectric in any phase and also found four temperature dependent modes by Raman scattering in the lowest temperature phase. Their frequencies decrease with increasing temperature towards room temperature. However, the mode assignment has not been made. In spite of these extensive experimental works on $CsPbCl_3$, the microscopic mechanism of three phase transitions in this crystal has not been clarified yet.

The purpose of the present work is to clarify the mechanism of the structural phase transitions in $CsPbCl_3$ by neutron scattering method.

For the later convenience, the phase transition schemes of $CsPbCl_3$ are shown in Fig.5. The symbols representing each phase and the transition temperature as indicated in the figure will be used hereafter. In §2, experimental methods of neutron

scattering and specific heat measurements are described. In §3, the observations of the temperature dependences of the Bragg reflections and the specific heat are described. These gave the overall feature of the successive phase transitions. In §4, the phonon dispersion curves in the cubic phase measured along the symmetric directions are given. The presence of the soft modes associated with the phase transitions is also shown. In §5, the mode determination of the condensing phonons is carried out by analyzing dynamical structure factors, and the space groups and the atomic arrangements at each phase are then inferred from the polarization vectors of the condensing modes. In §6, a phenomenological theory to explain the successive phase transitions caused by the condensation of the particular phonon modes is developed. It is shown that by a suitable choice of parameters included in the free energy expression, the observed phase schemes are qualitatively explained. In §7, the relation between the observed NQR spectra and the space groups determined in §5 is discussed. A microscopic origin of the successive phase transitions is also discussed on the basis of the lattice dynamical characteristics of perovskite crystal.

§2. Experimental

All single crystals used for the present experiments were kindly provided by Dr. S. Hirotsu of Tokyo Institute of Technology.

(i) Neutron scattering

The earlier part of the present neutron scattering experiments was carried out with the triple-axis neutron spectrometer (ISSP ND-1) installed at the JRR-2 reactor of Japan Atomic Energy Research Institute. The energy of incident neutrons was 14.2meV (2.40Å) from a pyrolytic graphite (002) monochromator. In this case, $\lambda/2$ components were eliminated with graphite filters. The germanium (111) plane was used for an analyzer. The collimation angles of four collimators; in-pile, monochromator to sample, sample to analyzer, analyzer to detector, are all 30min. The constant "Q" technique was utilized. The sample crystal has a nearly quadrangular pyramid shape with 1.2cc in volume and 15mm in height, and its mosaic spread was measured to be 0.4°. The specimen was set in the electric furnace and the temperature of the specimen was controlled within $\pm$0.2°.

Extensive measurements were also carried out on a triple-axis neutron spectrometer at the High Flux Beam Reactor of Brookhaven National Laboratory. Pyrolytic graphite (002) planes were used for both the monochromator and the analyzer. The inelastic scattering experiments were carried out with the incident energy of 38meV and all four collimations were 20min. On the other hand, most measurements of quasi-elastic scattering were made

with incident energy of 13.7meV and $\lambda/2$ components were eliminated with graphite filters. The collimation was 20min. before the monochromator and other three collimations were 40min. The crystal specimen has a nearly triangular pyramid shape with about 1cc in volume. The temperature of the specimen was kept constant within $\pm 0.2°$.

(ii) Specific heat measurements

The specific heat was measured by an a.c. calorimetry, technique recently developed. The principles of the a.c. calorimetry and the measuring system of this calorimeter have been reported in detail by Hatta and Ikushima.[21] The single crystal of 50μ in thickness and $2 \times 2 mm^2$ in area was blacked on one side with a graphite suspension to absorb the heat given by light pulses. A response of the periodic heating of the specimen was detected by one of two 25μ Chromel-Alumel thermocouples attached on the opposite side of the specimen to that exposed to the light. The other thermocouple detected the temperature of the specimen. The a.c. components of the response which are proportional to the inverse of the specific heat were plotted against temperature of the specimen. The heating rate of the specimen was 1°/7min.

§3. Successive Phase Transitions

Since it has been known that $CsPbCl_3$ was not ferroelectric,[20] we inferred that the phase transitions would be associated with zone boundary phonons. In fact, we observed superlattice Bragg reflections at the M-point $(\frac{1}{2},\frac{1}{2},0)$ and R-point $(\frac{1}{2},\frac{1}{2},\frac{1}{2})$ referred to the reciprocal lattice of the simple cubic lattice at room temperature(Fig.1). The temperature dependences of the intensities of superlattice reflections $\frac{3}{2}\ \frac{1}{2}\ 0$ and $\frac{3}{2}\ \frac{3}{2}\ \frac{5}{2}$ observed by neutron scattering are shown in Fig.6. The $\frac{3}{2}\ \frac{1}{2}\ 0$ reflection shows a distinct discontinuities at 47°C and then vanishes above this temperature. The $\frac{3}{2}\ \frac{3}{2}\ \frac{5}{2}$ reflection gradually decreases its intensity with increasing temperature and vanishes at 42°C. It also indicates slight discontinuity at 37°C. According to the earlier x-ray work by Sakudo et al.,[15] the superlattice reflections appear at the X-point $(0,0,\frac{1}{2})$ at room temperature. Therefore, the temperature dependence of the $1\ 1\ \frac{3}{2}$ reflection at the X-point was also measured. As is shown in Fig.6, the temperature dependence of the $1\ 1\ \frac{3}{2}$ reflection is similar to that of the $\frac{3}{2}\ \frac{3}{2}\ \frac{5}{2}$ reflection. Recently, Harada et al.[22] carried out the precise x-ray diffraction experiments and observed superlattice reflections at all points of X, M and R at room temperature, which is consistent with the present investigation. These temperature dependences of superlattice reflections clearly show the existence of three phase transitions and that the transition at 42°C would be of the second order and remaining two of the first order. These transitions are also identified by specific heat measurements. Fig.7 shows the spe-

cific heat versus temperature curve measured by the a.c. calorimetry method.

§4. Phonon Dispersions

The experimental results in the previous section suggest that the instabilities of the zone boundary phonons at the M-point and the R-point as observed in $KMnF_3$[9-11] and $NaNbO_3$[12] may occur at 47°C and 42°C in $CsPbCl_3$, respectively. In order to investigate the behavior of these phonons in the cubic phase, the phonon dispersion curves along the three symmetric directions [00ζ], [ζζ0] and [ζζζ] were measured by neutron inelastic scattering method. Fig.8 shows the phonon dispersion curves of the acoustic branches at 80°C(Phase I). It is characteristic of $CsPbCl_3$ crystal that the energy of the whole acoustic phonon is remarkably low in comparison with other perovskite crystals such as $SrTiO_3$[5] and $KMnF_3$.[9-11] Moreover, the longitudinal acoustic phonons with the energies larger than about 5 meV are broadened out and become unobserved along any one of three directions.

The energies of the Σ_3(TA) and the Λ_3(TA) branches along [ζζ0] and [ζζζ] which are compatible with the zone boundary modes M_3 and R_{25} tend to decrease at $\zeta \sim 0.3$ and in the range of $\zeta > 0.35$ they become overdamped. The quasi-elastic scatterings due to these overdamped phonons at their zone boundaries were observed at various temperatures. The measurement was made under the conditions that the crystal was mounted with the [1$\bar{1}$0] axis vertical so as to observe either the M_3 and R_{25} modes. Figs.9

and 10 show the temperature dependences of the quasi-elastic scattering at the M-point$(\frac{3}{2},\frac{1}{2},0)$ and the R-point$(\frac{3}{2},\frac{1}{2},\frac{1}{2})$, respectively. The energy resolutions were 0.16 meV FWHM in both cases, which are shown by the triangles in the figures. Since the low lying modes are overdamped around the M-point and R-point, it is impossible to observe the softening directly. However, we can estimate the frequency of the phonons as follows: It is known that when the neutron scattering cross section $(\frac{\partial^2\sigma}{\partial\Omega\partial\omega})$ due to excitation of an anharmonic phonon is integrated over ω, the resultant cross section $(\frac{\partial\sigma}{\partial\Omega})$ depends only on the characteristic frequency of the phonon, ω_0, and is independent of its damping constant.[23] Namely, the cross section is expressed by

$$(\frac{\partial\sigma}{\partial\Omega}) \propto k_B T \sum_j \frac{|F_d^j(K)|^2}{\omega_0^2(jq)} , \tag{1}$$

$$K = \tau + q, \tag{2}$$

where K is the scattering vector, τ the reciprocal lattice vector and q the reduced wave number vector. The dynamical structure factor $F_d^j(K)$ of the j-th phonon mode takes the form of

$$F_d^j(K) = \sum_\kappa \frac{b_\kappa}{\sqrt{m_\kappa}} K\cdot e_\kappa(jq)\ e^{-M_\kappa} e^{iK\cdot r_\kappa} , \tag{3}$$

$$M_\kappa = B_\kappa (\frac{\sin\theta}{\lambda})^2, \tag{4}$$

where b_κ, m_κ, B_κ and r_κ mean the scattering length, the mass, the isotropic temperature factor and the averaged position of the

κ-th atom in a unit cell, respectively. $e_\kappa(jq)$ is the polarization vector of the κ-th atom for the mode q of the j-th phonon branch.

The intensities integrated over the energy obtained from Figs.9 and 10 were analyzed with Eq.(1) to give the temperature dependence of ω_0. It was found that in each case the values of $T/(\frac{\partial\sigma}{\partial\Omega})$ changed nearly linearly against the temperature T and its extrapolation towards the lower temperature side became zero at T_0 which is lower than T_C. These represent that the undamped phonon energy of each mode decreases in proportion to $(T-T_0)$ as the temperature is lowered to the transition temperatures.

At the same time, the quasi-elastic scattering shows a remarkable anisotropy in the q-space. It extends from the M-point$(\frac{3}{2},\frac{1}{2},0)$ towards the R-point$(\frac{3}{2},\frac{1}{2},\frac{1}{2})$ in the cubic phase. In Fig.11, the intensity of the quasi-elastic scattering observed along the $[\frac{3}{2}\ \frac{1}{2}\ \zeta]$ direction with $q=(\frac{1}{2}\ \frac{1}{2}\ \zeta)$ connecting the M-point with the R-point is plotted by the solid circles(56°C) and triangles(80°C). The open circles and triangles in the same figure show the intensity of the quasi-elastic scattering along the $[\frac{3}{2}+\zeta\ \ \frac{1}{2}+\frac{\zeta}{3}\ \ 0]$ direction which is perpendicular to the $[\frac{3}{2}\ \frac{1}{2}\ \zeta]$ direction in the $(1\bar{3}0)$ plane used for this measurement. The origin in the figure corresponds to the M-point$(\frac{3}{2},\frac{1}{2},0)$. The wave number resolutions were 0.016 $\mathring{A}^{-1}$ FWHM along the $[\frac{3}{2}\ \frac{1}{2}\ \zeta]$ and 0.035 $\mathring{A}^{-1}$ FWHM along the $[\frac{3}{2}+\zeta\ \ \frac{1}{2}+\frac{\zeta}{3}\ \ 0]$ which are shown by the large solid and open triangles, respectively. The distance between the M-point and R-point is 0.566 $\mathring{A}^{-1}$ at 80°C. It is seen that the quasi-elastic scattering shows the ridge along the

$[\frac{3}{2}\ \frac{1}{2}\ \zeta]$ direction. Taking the difference of the resolution functions into consideration, the quasi-elastic scattering around the M-point is expected to be even more anisotropic than that directly observed. This fact represents that all phonons belonging to the T_2 mode along the $[\frac{1}{2}\ \frac{1}{2}\ \zeta]$ direction are overdamped and their energies are as low as those of the overdamped phonons at the M-point and R-point.

§5. Mode Determination and the Static Structures

Fig.12 shows the temperature dependence of the intensities of both the quasi-elastic scattering(open circles) and the Bragg reflection(solid circles) at the M-point$(\frac{3}{2},\frac{1}{2},0)$. It is seen that the intensity of the quasi-elastic scattering increases with decreasing temperature showing critical behavior. Since the Σ_3 phonon branch which is overdamped is compatible with M_3 at $\frac{1}{2},\frac{1}{2},0$, one can reasonably infer that the condensing mode is M_3. In order to determine the mode of the M-point uniquely, the intensity measurements of the quasi-elastic scatterings due to the soft (overdamped) phonon mode were made at the zone boundaries along the [110] direction around various reciprocal lattice points. Fig.13 shows the comparison between the observed(open circles) and calculated(solid circles) dynamical structure factors for various M-points at 80°C. In the calculation of the dynamical structure factors from Eq.(1), we used the eigen vectors of the M_3 mode illustrated in Fig.3(b). The temperature factor of

the chlorine atom defined by Eq.(4) which gave the best fitting between the observed and the calculated dynamical structure factors was 12.6 $\mathring{A}^2$ at 80°C. From this satisfactory agreement of the dynamical structure factors, it is concluded that the phase transition at 47°C is caused by the condensation of the M_3, [110] zone boundary mode. Below 47°C, the atomic displacement corresponding to the polarization of the M_3 mode takes place. The space group of the static structure at Phase II (42°C<T<47°C) due to the condensation of the M_3 mode was determined as D_{4h}^5-P4/nbm (see Fig.3 and Table I). The directions of the new principal axes of the tetragonal lattice, $[100]_t$, $[010]_t$ and $[001]_t$, are taken along [110], $[\bar{1}10]$ and [001] referred to the pseudo-cubic lattice, respectively. Then the unit cell is doubled ($\sqrt{2}a \times \sqrt{2}a \times a$) as compared with the cubic cell ($a \times a \times a$). It is well known that the rotation angle of the $PbCl_6$ octahedra around the $[001]_t$ axis plays a role of the order parameter in Phase II. This rotation is expressed as $\langle\phi_z'\rangle$. In this phase, the site symmetry of the Cl_I ion is different from that of the Cl_{II} and Cl_{III} ions which are placed at the equivalent sites as shown in Fig.2(c), while in Phase I all Cl ions are placed at the equivalent sites.

In the cubic phase, it has been observed that the Λ_3 branch which is compatible with the R_{25} mode at $\frac{1}{2},\frac{1}{2},\frac{1}{2}$ was also overdamped. Following the same procedure as the case of the M_3 mode, observed quasi-elastic intensities at various R-points were compared with the calculated dynamical structure factors using the eigen vectors of the R_{25} mode illustrated in

Fig.2(a). The temperature factor giving the best fitting was 10.5 $\mathring{A}^2$ at 55°C where quasi-elastic scatterings were measured. As is shown in Fig.14, agreement between observation and calculation is satisfactory, from which we may infer that the condensing mode at 42°C is R_{25}. However, the preceding phase transition to the tetragonal phase at 47°C causes some complications in mode assignments. In Fig.15, the temperature dependences of quasi-elastic scattering and the Bragg reflection at $\frac{3}{2},\frac{3}{2},\frac{5}{2}$ are shown. It is observed that the quasi-elastic scattering diverges at 42°C corresponding to the expected condensation of R_{25} mode. Further, it is noticed that the quasi-elastic scattering shows a sudden increase at the transition point, 47°C. This could be interpreated due to the fact that the triply degenerate R_{25} mode in the cubic phase splits into the doubly degenerate Z_5 mode and the non-degenerate Z_1 mode in the tetragonal phase. Another effect of the tetragonality in Phase II can be seen in the appearance of quasi-elastic scattering at the X-point (referred to the cubic lattice) in the tetragonal phase. Fig.16 shows the temperature dependences of the quasi-elastic scattering and the Bragg reflection at $1,1,\frac{3}{2}$. Below 47°C, similar temperature dependences as those of R-point are seen (cf. Fig.15). This is simply because of the fact that in the tetragonal phase, the R-points and the X-points referred to the cubic lattice become equivalent, both being the Z-points of the tetragonal unit cell. In Fig.17, the reciprocal lattice of the tetragonal system is shown together with that of the cubic system.

In order to investigate how the R_{25} normal mode at the

R-point in the cubic perovskite crystal is modified under the influence of the tetragonality, the normal mode analysis in the tetragonal lattice with the space group D_{4h}^5- P4/mbm was made at the Z-point, the zone boundary along the tetragonal $[001]_t$ direction. The unit cell involves ten ions. At the Z-point, the little group is 4/mmm, and the irreducible representations are obtained as

$$3Z_1 + Z_1' + 2Z_2 + Z_3 + Z_3' + 2Z_4 + 2Z_4' + 5Z_5 + 4Z_5' .$$

Here, Z_5 and Z_5' correspond to doubly degenerate modes. It is found that the doubly degenerate mode representing the rotational vibration of the $PbCl_6$ octahedra around the pseudo-cubic axes [100] and [010] belongs to the Z_5 mode and the other non-degenerate mode whose axis of rotation is along the [001] direction belongs to the Z_1 mode. These are not purely rotational mode but are accompanied by the displacements of the other ions. The Z_1 mode represents the rotational vibration of the $PbCl_6$ octahedra around the [001] axis accompanied by the displacements of the both ions Cs and Cl_I along the [001] direction. The Z_5 mode, on the other hand, is accompanied by the displacements of the Cs ion along the rotation axis of the octahedra. Since the tetragonality modifies the vibrational spectra only slightly, one can assume that the overdamped mode at Z-point is either one of these rotational modes. Further the optical measurements[19] have shown that the crystal symmetry in Phase III was lower than orthorhombic. Therefore, we infer that the condensing mode is

the doubly degenerate mode belonging to Z_5, whose rotation angle is perpendicular to the tetragonal unique axis. To specify each of the degenerate mode, let us use the symbols Z_5^x and Z_5^y. For the Z_5^x and Z_5^y modes, dynamical structure factors at the X-point and R-point referred to the pseudo-cubic lattice are given by

$$|F_d^x(X)| \propto \left|\frac{b_{Cl}}{\sqrt{m_{Cl}}}\pi\langle\phi_z'\rangle\ \phi_x\ (-1)^{\ell}\ (\ell+\tfrac{1}{2})h\ e^{-M_{Cl}}\right.$$
$$\left. + \frac{b_{Cs}}{\sqrt{m_{Cs}}}\ (U_x+U_x')\,(-1)^{\ell}\ h\ e^{-M_{Cs}}\right|, \qquad (5)$$

$$|F_d^y(X)| \propto \left|\frac{b_{Cl}}{\sqrt{m_{Cl}}}\pi\langle\phi_z'\rangle\ \phi_y\ (-1)^{\ell}\ (\ell+\tfrac{1}{2})k\ e^{-M_{Cl}}\right.$$
$$\left. + \frac{b_{Cs}}{\sqrt{m_{Cs}}}\ (U_y+U_y')\,(-1)^{\ell}\ k\ e^{-M_{Cs}}\right|, \qquad (6)$$

$$|F_d^x(R)| \propto \left|\frac{b_{Cl}}{\sqrt{m_{Cl}}}\phi_x\{(-1)^{k+\ell}(k+\tfrac{1}{2}) - (\ell+\tfrac{1}{2})\}e^{-M_{Cl}}\right.$$
$$\left. + \frac{b_{Cs}}{\sqrt{m_{Cs}}}\ (U_x-U_x')\,(-1)^{\ell}\ (h+\tfrac{1}{2})e^{-M_{Cs}}\right|, \qquad (7)$$

$$|F_d^y(R)| \propto \left|\frac{b_{Cl}}{\sqrt{m_{Cl}}}\phi_y\{(-1)^{h+\ell}(h+\tfrac{1}{2}) - (\ell+\tfrac{1}{2})\}e^{-M_{Cl}}\right.$$
$$\left. + \frac{b_{Cs}}{\sqrt{m_{Cs}}}\ (U_y-U_y')\,(-1)^{\ell}\ (k+\tfrac{1}{2})e^{-M_{Cs}}\right|. \qquad (8)$$

Here, ϕ_x and ϕ_y represent the angle of rotation of the $PbCl_6$ octahedra around [100] and [010], respectively. U_x and U_y are the eigen vectors along [100] and [010] of the Cs_I ion, and U_x' and U_y' are those of Cs_{II} ion. h, k and ℓ represent the indices of the reciprocal lattice points referred to the pseudo-cubic lattice.

These formula are obtained by the linear expansion of Eq.(3) with respect to $\langle\phi'_z\rangle$. It is noticed that $F_d(X)$ is linear to $\langle\phi'_z\rangle$ so the tetragonality of the lattice gives rise to new quasi-elastic scattering at the X-point, but no influence to that at the R-point can be occured by the tetragonality under the above approximation. In Phase I, $\langle\phi'_z\rangle$ as well as U and U' becomes zero. Therefore, $F_d(X)$ becomes zero while $F_d(R)$ has a finite value even above 47°C, which agrees well with the experimental results shown in Figs.15 and 16. The dynamical structure factors obtained from the quasi-elastic scatterings at the X-point and R-point measured at 45°C (Phase II) are shown in Figs.18 and 19, respectively. The open circles in the figures represent the experimental values. In the calculation of the dynamical structure factors, Eqs.(5)-(8) are rewritten on the assumption of $M_{Cl}=M_{Cs}$ as

$$|F_d^x(X)| \propto |(-1)^{\ell}(\ell+\tfrac{1}{2})h + \alpha(-1)^{\ell} h|\, e^{-M_{Cl}}, \tag{9}$$

$$|F_d^y(X)| \propto |(-1)^{\ell}(\ell+\tfrac{1}{2})k + \alpha(-1)^{\ell} k|\, e^{-M_{Cl}}, \tag{10}$$

$$|F_d^x(R)| \propto |\{(-1)^{k+\ell}(k+\tfrac{1}{2}) - (\ell+\tfrac{1}{2})\} + \beta(-1)^{\ell}(h+\tfrac{1}{2})|\, e^{-M_{Cl}}, \tag{11}$$

$$|F_d^y(R)| \propto |\{(-1)^{h+\ell}(h+\tfrac{1}{2}) - (\ell+\tfrac{1}{2})\} + \beta(-1)^{\ell}(k+\tfrac{1}{2})|\, e^{-M_{Cl}}, \tag{12}$$

where α and β are taken as parameters. α is determined so as to give the best fitting between the observed and calculated intensities. The same temperature factor of B_{Cl} as is obtained at 55°C was used. The calculated dynamical structure factors at the

X-point in the case of $\alpha=0.4$ are shown by the solid circles in Fig.18. As for the R-point, β is smaller than α by a factor of $\pi\langle\phi'_z\rangle$ so that the second term in Eqs.(11) and (12) is negligibly small in comparison with the first term. The calculated values at the R-point are shown by the solid circles in Fig.19. In both cases, the effect of the domains was taken into account assuming that they are equally distributed. The agreement between the observed and the calculated dynamical structure factors is satisfactory.

The space group of the crystal structure of Phase III attained by the condensation of the Z_5^x mode was determined to be D_{2h}^{17}- Cmcm. In this space group, the directions of the new principal axes of the orthorhombic lattice $[100]_o$, $[010]_o$ and $[001]_o$ are taken along the directions [010], [100] and $[00\bar{1}]$ referred to the pseudo-cubic lattice, respectively. The unit cell becomes eight-fold (2a x 2a x 2a) in comparison with the cubic cell (a x a x a). In this phase, the Cl_I, Cl_{II} and Cl_{III} ions are placed at non-equivalent sites(Fig.20).

As for the phase transition at 37°C, the same procedure as used to determine the condensing mode for the transitions at 47°C and 42°C cannot be followed because the quasi-elastic scattering is masked by the strong Bragg reflection which already exists at Z-points. However, we have observed that the intensities of the Bragg reflections at room temperature (Phase IV) at Z-points were proportional to those of the quasi-elastic scatterings at 45°C. This means that the eigen vectors of the soft mode which causes the phase transition at 37°C should be similar

to that of the Z_5 mode. In fact, it is found from Eqs.(9)-(12) that the dynamical structure factors F_d^x and F_d^y due to the modes Z_5^x and Z_5^y give the same intensities at the reciprocal lattice points where the observations are made. Therefore, the phase transition at 37°C is caused by the condensation of the remaining Z_5^y mode. The crystal structure of Phase IV is shown in Fig.21. The space group was determined as C_{2h}^2- $P2_1/m$. The directions of the new principal axes of the monoclinic lattice $[100]_m$, $[010]_m$ and $[001]_m$ are taken along the directions [110], [001] and $[\bar{1}10]$ referred to the pseudo-cubic lattice when the $[010]_m$ axis is taken as a unique axis. The unit cell is quadrupled ($\sqrt{2}a \times 2a \times \sqrt{2}a$) in comparison with the cubic cell. It is found that the Cl_{II} and Cl_{III} ions have very similar ionic arrangements around themselves though they are not crystallographically equivalent.

§6. Phenomenological Treatment of Successive Phase Transitions in $CsPbCl_3$

The three successive phase transitions in $CsPbCl_3$ show interesting correspondence to the phase transitions in $BaTiO_3$[4]. In the case of $BaTiO_3$, the phase transitions are caused by the successive condensations of each of triply degenerate optical active modes at the zone center. In the case of $CsPbCl_3$, on the other hand, the phase transitions are caused by the successive condensations of the zone boundary modes associated with the rotational vibration of the $PbCl_6$ octahedra around the principal axes of the cubic lattice. The three axial vectors describing the rotation of the $PbCl_6$ octahedra around the principal axis play the role of the order parameters in $CsPbCl_6$ in contrast with the case of $BaTiO_3$ where three polar vectors (components of the spontaneous polarization) play the same role. However, in $CsPbCl_3$ it should be noticed that there are four independent order parameters associated with the non-degenerate M_3 and triply degenerate R_{25} modes. The amplitudes of these four rotational modes are expressed as ϕ'_z, ϕ_x, ϕ_y and ϕ_z. On the analogy of the Devonshire theory for $BaTiO_3$[2,4], the free energy is expanded up to the sixth order with respect to the rotation angles as follows:

$$F = \frac{\chi'}{2}\phi_z'^2 + \frac{\chi}{2}(\phi_x^2 + \phi_y^2 + \phi_z^2) + \frac{C}{4}\phi_z'^4 + \frac{D}{4}(\phi_x^4 + \phi_y^4 + \phi_z^4)$$

$$+ \frac{E}{2}(\phi_x^2\phi_y^2 + \phi_y^2\phi_z^2 + \phi_z^2\phi_x^2) + \frac{F}{2}\phi_z'^2(\phi_x^2 + \phi_y^2)$$

$$+ \frac{F'}{2}\phi_z'^2\phi_z^2 + \frac{G}{6}\phi_z'^6 + \frac{H}{4}\phi_z'^2(\phi_x^4 + \phi_y^4) + \frac{H'}{4}\phi_z'^2\phi_z^4$$

$$+ \frac{I}{2}\phi_z'^2\phi_x^2\phi_y^2 + \frac{K}{2}\phi_x^2\phi_y^2\phi_z^2 + \frac{L}{2}\phi_z'^2\phi_z^2(\phi_x^2 + \phi_y^2). \qquad (13)$$

As is usually done, we assume that the coefficients in this expansion have the symmetry property of the cubic phase, and that all of them except χ' and χ are independent of temperature. χ' and χ take the form of

$$\chi' = A(T - T_0') \qquad (A > 0), \qquad (14)$$

$$\chi = B(T - T_0) \qquad (B > 0). \qquad (15)$$

T_0' and T_0 are certain temperatures related to the intrinsic transition temperatures of the phase transitions caused by the condensation of the M_3 and R_{25} modes, respectively. The stability conditions of the system at an arbitrary temperature are given by

$$\frac{\partial F}{\partial \phi_z'} = \frac{\partial F}{\partial \phi_x} = \frac{\partial F}{\partial \phi_y} = \frac{\partial F}{\partial \phi_z} = 0. \qquad (16)$$

At the present stage, one cannot determine the coefficients in (13) quantitatively. Therefore, we investigate only the following four solutions which represent the four phases actually observed in $CsPbCl_3$.

(i) $\phi_z' = \phi_x = \phi_y = \phi_z = 0$ (Phase I),

(ii) $\phi_z' \neq 0,\ \phi_x = \phi_y = \phi_z = 0$ (Phase II),

(iii) $\phi_z' \neq 0,\ \phi_x \neq 0,\ \phi_y = \phi_z = 0$ (Phase III),

(iv) $\phi_z' \neq 0,\ \phi_x = \phi_y \neq 0,\ \phi_z = 0$ (Phase IV).

A. Phase I and Phase II

In Phase I, the minumum of the free energy is given by the condition (i). If we assume that $T_0' > T_0$, the system will become stable with the condition (ii). In Phase II, the free energy is expressed as

$$F_{II} = \frac{\chi'}{2}\phi_z'^2 + \frac{C}{4}\phi_z'^4 + \frac{G}{6}\phi_z'^6. \tag{17}$$

As is well known, the condition that the transition is of the first order as actually observed in $CsPbCl_3$ is

$$C < 0, \quad G > 0. \tag{18}$$

The rotation angle ϕ_z' is given by

$$\phi_z'^2 = \frac{1}{2G}\{-C + \sqrt{C^2 - 4GA(T - T_0')}\}. \tag{19}$$

Substituting Eq.(19) into (17), the transition temperature T_I is obtained from the equation

$$\chi_0' \equiv A(T_I - T_0') = 3C^2/16G. \tag{20}$$

Corresponding to the first order transition, the value of ϕ_z' shows finite jump at T_I which is given by

$$\phi_{z0}'^2 = -3C/4G. \tag{21}$$

From Eqs.(20) and (21), we obtain

$$C = -4\chi_0'/\ \phi_{z0}'^2\ , \tag{22}$$

$$G = 3\chi_0'\ /\ \phi_{z0}'^4\ . \tag{23}$$

These values should be determined from the experimental data.

B. Phase III and Phase IV

To investigate the phase transitions associated with the condensation of Z_5 mode, we proceed as follows: Let us assume that the order parameter ϕ_z' is not affected very much by the onset of the phase transitions under consideration. In fact, the experimental results show that this assumption is actually satisfied since the Bragg intensity at M-point shows little disturbances at the lower two transition points (Fig.6). On this assumption, ϕ_z' is looked upon as a temperature dependent parameter, not a thermodynamical variable, whose temperature depend-

ence is simply determined by Eq.(19). This parameter is expressed as $\langle\phi'_z\rangle$. Further, we assume that the parameters D, F' and H' are positive, so that the equilibrium state is always attained with $\phi_z=0$ throughout the temperature region we are concerned. The free energy is then given by

$$F = F_{II} + \frac{B'}{2}(\phi_x^2 + \phi_y^2) + \frac{D'}{4}(\phi_x^4 + \phi_y^4) + \frac{E'}{2}\phi_x^2\phi_y^2 \ , \qquad (24)$$

with

$$B' = \chi + F\langle\phi'_z\rangle^2 \ , \qquad (25)$$

$$D' = D + H\langle\phi'_z\rangle^2 \ , \qquad (26)$$

$$E' = E + I\langle\phi'_z\rangle^2 \ . \qquad (27)$$

It is noted that the coefficients D' and E' are now temperature dependent through $\langle\phi'_z\rangle$. The stability conditions

$$\frac{\partial F}{\partial \phi_x} = \frac{\partial F}{\partial \phi_y} = 0 \qquad (28)$$

allow us two sets of solutions, ($\phi_x\neq 0$, $\phi_y=0$) and ($\phi_x=\phi_y\neq 0$), with finite values of order parameters depending on the values of the coefficients D' and E'. These solutions exactly correspond to the observed phase III and IV. The order parameters and the free energies for the respective phases are given by

$$\phi_x^2(III) = -B' \ / \ D' \ , \qquad (29)$$

$$F_{III} = F_{II} - B'^2/4D' \ , \tag{30}$$

$$\phi_x^2(IV) = \phi_y^2(IV) = -B'/(D' + E') , \tag{31}$$

$$F_{IV} = F_{II} - B'^2/2(D' + E') . \tag{32}$$

To obtain stable states in lower temperatures, we have

$$B' < 0 \ , \tag{33}$$

$$D' > 0 \ , \tag{34}$$

$$D' + E' > 0 \ . \tag{35}$$

In Fig.22, a schematic diagram of the free energy curve at each phase is shown. The conditions that F_{III} is lower than F_{IV} in the temperature range of $T>T_{III}$ and F_{IV} is lower than F_{III} in the range of $T<T_{III}$ as actually observed in $CsPbCl_3$ are

$$D' < E' \quad \text{for} \quad T > T_{III} \ , \tag{36}$$

$$D' = E' \quad \text{for} \quad T = T_{III} \ , \tag{37}$$

$$D' > E' \quad \text{for} \quad T < T_{III} \ . \tag{38}$$

The transition temperature T_{III} between Phase III and Phase IV is determined from Eq.(37). Using Eqs.(26) and (27), the conditions (36) and (38) are rewritten as

$$D - E < (I - H)\langle\phi_z'\rangle^2 \quad \text{for} \quad T > T_{III} , \tag{39}$$

$$D - E > (I - H)\langle\phi_z'\rangle^2 \quad \text{for} \quad T < T_{III} . \tag{40}$$

As the parameter $\langle\phi_z'\rangle$ monotonically decreases and tends to zero with increasing temperature, the condition that the temperature independent parameters D-E and I-H satisfy the inequalities (39) and (40) is given by

$$H - I > 0 > D - E . \tag{41}$$

In Fig.23, the stable region of these phases with respect to D' and E' is mapped out. The stable state at an arbitrary temperature is represented by the point (D',E') with $D'=D+H\langle\phi_z'\rangle^2$ and $E'=E+I\langle\phi_z'\rangle^2$. Eliminating $\langle\phi_z'\rangle^2$, we have

$$E' = \frac{I}{H} D' + (E - \frac{I}{H} D). \tag{42}$$

This means that the representative point of the system moves along the straight line given by the above formula in D'-E' plane. As the line (42) and the line D'=E' intersect at $D'=E'=\frac{EH-DI}{H-I}$ where $T=T_{III}$, one can obtain one more condition

$$EH - DI > 0 \tag{43}$$

because of the occurrence of the phase transition between Phase III and Phase IV under the conditions (34) and (35).

The conditions (41), (43) and D>0 show that the point comes across the boundary of these two different regions in the way that is shown by the arrow in Fig.23 as the temperature is lowered.

Summarizing, one can obtain the following equations and inequalities to determine various parameters to explain the observed successive phase transitions.

(i) $A(T_I - T_0') = 3C^2/16G$,

(ii) $B(T_{II} - T_0) + F\langle\phi_z'(T_{II})\rangle^2 = 0$,

(iii) $D - E = (I - H)\langle\phi_z'(T_{III})\rangle^2$,

(iv) $A > 0, \quad B > 0$,

(v) $C < 0, \quad G > 0$,

(vi) $E > D > 0$,

(vii) $H > I$,

(viii) $EH - DI > 0$,

(ix) $B' < 0, \quad D' > 0, \quad D' + E' > 0$.

In order to determine the set of coefficients numerically, more experiments should be carried out. It is noted, however, that there is a simple relation between the Bragg intensity at the X-point in Phase III and that of Phase IV at T_{III}, irrespective of the numerical values of the coefficients. Substituting the relation D'=E' into Eqs.(29) and (31), we can obtain the order parameters at T_{III} in both Phase III and IV as follows

$$\phi_x^2(III) = -B'/D' \ , \tag{44}$$

$$\phi_x^2(\mathrm{IV}) = \phi_y^2(\mathrm{IV}) = -B'/2D'. \tag{45}$$

Calculating the static structure factors F_s on the basis of the crystal structure determined in §5, we obtain

$$F_s \propto (\phi_x + \phi_y) , \tag{46}$$

for the h h $\ell+\frac{1}{2}$ type reflections referred to the cubic lattice as used in the present experiment (see Fig.6). Then the intensity just above T_{III} in Phase III is

$$I(\mathrm{III}) \propto \phi_x^2(\mathrm{III}) = -B'/D' . \tag{47}$$

On the other hand, the intensity just below T_{III} in Phase IV is

$$I(\mathrm{IV}) \propto (\phi_x + \phi_y)^2 = 4\phi_x^2(\mathrm{IV}) = -2B'/D' = 2\, I(\mathrm{III}). \tag{48}$$

This rough estimation of the change in the Bragg intensities at T_{III} (Fig.24) is qualitatively consistent with the experimental results shown in Fig.6.

§7. Discussion

Since the superlattice reflections at X-points (referred to the cubic lattice) were observed by Sakudo et al.[15], it has been conjectured that there exists a certain soft zone boundary mode at X-point in the cubic phase in addition to the rotational modes. However, the observed TA phonon dispersion at the X-point (Fig.8) is well defined and shows no temperature dependence in the temperature range from 80°C to 45°C. Further the analysis of the quasi-elastic scattering at the same point shows that the overdamped mode at X-point is associated with the Z_5 mode which is derived from the R_{25} mode. Therefore, the phase transitions of $CsPbCl_3$ are interpreted as in the common basis of the softening of the rotational modes which are characteristic of the perovskite structure.

The symmetry properties at each phase determined by the present investigation are compared with the NQR spectra on Cl^- ion measured by Jensen using the powder specimen (Fig.4).[4] In Phase I (Fig.1), all Cl ions are placed at the equivalent 3d sites with the site symmetry 4/mmm shown in Table I so that they have the same field gradient. This explains the observed single NQR line above 47°C in Phase I shown in Fig.4. In Phase II (Fig.3), Cl_{II} and Cl_{III} ions are placed at the equivalent 4f site with the site symmetry mm. On the other hand, Cl_I ion which does not move by the rotation of the $PbCl_6$ octahedron around the [001] axis, is placed at the 2b site with the site symmetry 4/m. Therefore, two NQR lines must appear in Phase II and moreover their intensity ratio is to be 2:1. This is consistent with

the experimental results. In Phase III (Fig.20), Cl_{II} and Cl_{III} ions become crystallographically non-equivalent owing to the rotation of the octahedra around the [100] axis. Cl_{II} ion has the site symmetry m while Cl_{III} has the site symmetry 2. In this case, it is noticed that Cl_{II} shifts out of the (001) plane containing the Pb ions while Cl_{III} is placed nearly on its plane, which results in that the distance between the Cl_{II} and its nearest neighboring Pb ions is substantially different from that between the Cl_{III} and its nearest neighboring Pb ions. As Pb ion gives rise to the large contribution to the field gradient of the Cl ion, the stronger NQR line should split into two lines with nearly equal intensities. This is also consistent with the experimental results in Phase III shown in Fig.4. In Phase IV(Fig.21), Cl_{III} also shifts out of the (001) plane containing the Pb ions while Cl_{III} stays at the nearly same position as in Phase III. Then the distance between the Cl_{III} and its nearest neighboring Pb ion becomes nearly equal to that for Cl_{III}. Moreover, as seen in Fig.21, the ionic arrangements around the Cl_{II} are found to be very similar to that around the Cl_{III}, although the Cl_{II} and Cl_{III} are crystallographically non-equivalent. Therefore, two lines which once split in Phase III may come close together in Phase IV. These two adjacent NQR lines may be observed as a single line if their splitting is within the resolution of the spectrometer. This situation is visualized more clearly by the following considerations. If we assume that at Phase II the rotation of the $PbCl_6$ octahedron around the [001] axis is infinitesimally small, the space group of the structure

stabilized by the condensation of the Z_5^x mode is D_{2h}^{23} - Fmmm. In this case, Cl_{II} and Cl_{III} are placed at non-equivalent sites (8h,8f). On the other hand, the condensation of $Z_5^x + Z_5^y$ gives the structure with the space group D_{2h}^{28} - Imma. In such a case, Cl_{II} and Cl_{III} are placed at the equivalent 8g sites. Therefore, when the rotation angle of the $PbCl_6$ octahedron caused by the condensation of the M_3 mode is small, Cl_{II} and Cl_{III} ions in Phase IV may be regarded as nearly equivalent. Thus, the site symmetry of the chlorine ions on the basis of the space group determined in the present work well explains the observed splittings of the NQR spectra at each phase.

The successive phase transitions observed in $CsPbCl_3$ as well as $KMnF_3$ and $NaNbO_3$ are caused by the condensation of the same zone boundary modes of M_3 and R_{25}. As the condensations of these modes are characteristic to the perovskite structure, the lattice dynamical property of this structure is investigated using the rigid ion model.[25] The force constants of short-range interaction are expressed by A_i and B_i which are the derivatives of a harmonic potential function parallel and perpendicular to the line joining the interacting ions, respectively. The suffix i runs from one to three where one is for A-X, two is for B-X and three is for X-X forces(see Fig.1). The equations of motion of the ions lead to the set of equations.

$$\sum_{\kappa'} \sum_{\beta} [D_{\alpha\beta}(\kappa\kappa') - m_{\kappa}^{\frac{1}{2}} m_{\kappa}^{\frac{1}{2}}, \omega^2 \delta_{\kappa\kappa} \delta_{\alpha\beta}] U_{\beta}(\kappa') = 0 , \qquad (49)$$

where m_κ is the mass of the κ ion and $U_\beta(\kappa')$ is the β component

of the polarization vector of the κ' ion. $D_{\alpha\beta}(\kappa\kappa')$ is the element of the dynamical matrix, which corresponds to the β component of the force acting on the κ' ion when the κ ion moves along the α direction. The secular equation is given by

$$\det \left| D_{\alpha\beta}(\kappa\kappa') - m_{\kappa}^{\frac{1}{2}} m_{\kappa'}^{\frac{1}{2}} \omega^2 \delta_{\kappa\kappa'}\delta_{\alpha\beta} \right| = 0 \ . \qquad (50)$$

The dimension of this determinant for the cubic perovskite is 15 x 15. For the symmetric direction of q, the left-hand side of Eq.(47) is easily factored so that the phonon energy of each mode can be explicitly expressed in terms of the force constants involved in the dynamical matrix. Now, we consider, in particular, the direction $[\frac{1}{2}\ \frac{1}{2}\ \zeta]$. The phonon energy of the T_2 branch, which connects M_3 to R_{25}, can be easily obtained as

$$\omega^2(T_2) = \frac{1}{m_X}\left[A_1+B_1+B_2+4B_3+\frac{Z_X^2 e^2}{v}\{C_1(\zeta) - C_2(\zeta)\}\right], \qquad (51)$$

where $C_1(\zeta)$ and $C_2(\zeta)$ are the Coulomb coefficients of $(B\text{-}B)_{xx}$ and $(A\text{-}X_I)_{xy}$ type shown in Table II, respectively. It is characteristic of $\omega(T_2)$ that the ζ-dependence of energy is due only to Coulombic term. The value of the Coulomb coefficient $C_1(\zeta)-C_2(\zeta)$ monotonically decreases along the $[\frac{1}{2}\ \frac{1}{2}\ \zeta]$ direction from -14.383 at $\zeta=0$ to -14.461 at $\zeta=1/2$ in units of $Z_X^2 e^2/v$. Therefore the difference between the $\omega^2(M_3)$ and $\omega^2(R_{25})$ is given by

$$\omega^2(M_3)-\omega^2(R_{25}) = 0.078\frac{Z_X^2 e^2}{m_X v} \ , \qquad (52)$$

where $Z_X e$ is the ionic charge of the X ion and v is the volume of a unit cell. In the case of $CsPbCl_3$, we obtain $\omega^2(M_3)-\omega^2(R_{25})$ $=0.8\ meV^2$, which means that the dispersion of the T_2 branch is very flat. This is consistent with the experimental result of the quasi-elastic scattering observed along the $[\frac{1}{2},\frac{1}{2},\zeta]$ direction (Fig.11). However, Eq.(52) shows that the R_{25} mode always lies lower than the M_3 mode, which conflicts with the experimental fact in $CsPbCl_3$ that the M_3 mode condenses at the higher temperature than the R_{25} mode. If we take the short-range interaction between the X ions belonging to the neighboring octahedra into account, the phonon energy of the T_2 mode is given by

$$\omega^2(T_2) = \frac{1}{m_X}[A_1+B_1+B_2+4B_3+2A_4+B_4(1-\cos 2\pi\zeta) + \frac{Z_X^2e^2}{v}\{C_1(\zeta)-C_2(\zeta)\}]. \quad (53)$$

Then, we obtain

$$\omega^2(M_3)-\omega^2(R_{25}) = \frac{1}{m_X}\left(-2B_4+0.078\frac{Z_X^2e^2}{v}\right). \quad (54)$$

By a suitable choice of the parameter B_4, the energy of the M_3 mode can be lower than R_{25}. However, it is not clear whether or not this parameter B_4 plays an essential role for the softening of the both modes M_3 and R_{25} because of the simplicity of a harmonic rigid ion model.

Møller[14] carried out the structure analysis of $CsPbCl_3$ by x-ray diffraction. He reported that the structure in the highest temperature phase was of the perovskite type with some disordered atomic arrangements in which the chlorine and cesium ions can take several equivalent positions slightly displaced from the ideal perovskite positions. According to his Fourier map, the chlorine ion occupies statistically four positions along the face diagonals, about 0.5 Å away from the face center. As for the cesium ion, the definite disordered position is not clearly seen on the Fourier map. A preliminary experiment of the neutron powder diffraction of $CsPbCl_3$ in its cubic phase made by the present author, has also shown similar results. The observed small transition entropy (0.25 $cal.mol.^{-1}deg^{-1}$) associated with the phase transition at 47°C[20] suggests that even if the positions of chlorine ions are disordered, they don't independently move around their disordered positions but rotate collectively so that the framework of the $PbCl_6$ octahedron remains rigid. This is closely related to the experimental fact that both modes M_3 and R_{25} representing the rotational vibration of the $PbCl_6$ octahedron are heavily overdamped.

Acknowledgements

The author wishes to express his sincere thanks to Prof. Y. Yamada of Osaka University for his continued encouragements, invaluable suggestions and discussions, and for his correcting the manuscript. The author would like to express his sincere thanks to Prof. S. Hoshino of Tokyo University for his continued encouragements and stimulating discussions, and his critical reading the manuscript. He is also very grateful to Dr. S. Hirotsu of Tokyo Institute of Technology for providing good single crystals and for valuable discussions. The author asked Prof. Y. Yamada, Dr. J. D. Axe and Dr. G. Shirane to make neutron scattering measurements at Brookhaven National Laboratory, and he expresses his deep thanks to them. The specific heat measurements were made in cooperation with Dr. S. Hirotsu and Prof. A. Ikushima of Tokyo University, to whom the author is much indebted. Thanks are also due to Prof. J. Harada of Nagoya University for many kind informations on his x-ray experimental data prior to publication and his discussions. I would like to acknowledge Dr. H. Motegi of Hiroshima University who gives me continuous hospitality, for his assisting experiments and his discussions.

References

1) J.Harada, J.D.Axe and G.Shirane: Phys. Rev. 4B(1971)155.

2) G.Shirane, J.D.Axe and J.Harada: Phys. Rev. 2B(1970)155.

3) J.D.Axe, J.Harada and G.Shirane: Phys. Rev. 1B(1970)1227.

4) W.J.Merz: Phys. Rev. 76(1949)1221.

5) G.Shirane and Y.Yamada: Phys. Rev. 177(1969)858.

6) J.D.Axe, G.Shirane and K.A.Müller: Phys. Rev. 183(1969)820.

7) H.Thomas and K.A.Müller: Phys. Rev. Letters 21(1968)1256.

8) E.Pytte and J.Feder: Phys. Rev. 187(1969)1077.

9) V.J.Minkiewicz and G.Shirane: J. Phys. Soc. Japan 26(1969)674.

10) G.Shirane, V.J.Minkiewicz and A.Linz: Solid State Commun. 8(1970)1941.

11) K.Gesi, J.D.Axe and G.Shirane: Phys. Rev. 5B(1972)1933.

12) K.Ishida and G.Honjo: J. Phys. Soc. Japan 30(1971)899, ibid. 32(1972)1441.

13) V.J.Minkiewicz, Y.Fujii and Y.Yamada: J. Phys. Soc. Japan 28(1970)443.

14) C.K.Møller: Mat. Fys. Medd. Danske Vidensk Selsk. 32(1959)No.2.

15) T.Sakudo, H.Unoki, Y.Fujii, J.Kobayashi and M.Yamada: Phys. Letters 28A(1969)542.

16) S.Hirotsu and S.Sawada: Phys. Letters 28A(1969)762.

17) N.Torberg-Jensen: J. chem. Phys. 50(1969)559.

18) J.A.Cape, R.L.White and R.S.Feigelson: J. appl. Phys. 40 (1969)5001.

19) S.Hirotsu: J. Phys. Soc. Japan 28(1970)185 Suppl.

20) S.Hirotsu: J. Phys. Soc. Japan 31(1973)552.

21) I.Hatta and A.Ikushima: J. Phys. Chem. Solids 34(1973)57.

22) H.Ōta, J.Harada and S.Hirotsu: private communications.

23) Y.Yamada and G.Shirane: Phys. Rev. 177(1969)848.

24) A.F.Devonshire: Phil. Mag. 40(1949)1040.

25) R.A.Cowley: Phys. Rev. 134(1964)981.

Table I

The crystal system and space groups at each phase of $CsPbCl_3$. The Wyckoff notations and point symmetries of equivalent positions are also shown.

Phase I (47°C<T)

cubic	O_h^1 - Pm3m		z = 1	a x a x a
	Pb	1 a	m3m	
	Cs	1 b	m3m	
	Cl	3 d	4/mmm	

Phase II (42°<T<47°C)

tetragonal	D_{4h}^5 - P4/mbm		z = 2	√2a x √2a x a
	Pb	2 a	4/m	
	Cs	2 c	mmm	
	Cl-I	2 b	4/m	
	Cl-II Cl-III	4 g	mm	

Phase III(37°<T<42°C)

orthorhombic	D_{2h}^{17} - Cmcm		z = 8	2a x 2a x 2a
	Pb	8 d	$\bar{1}$	
	Cs	4 c	mm	
		4 c'		
	Cl-I	8 g	m	
	Cl-II	8 f	m	
	Cl-III	8 e	2	

Phase IV (T<37°C)

monoclinic	C_{2h}^2 - $P2_1/m$		z = 4	√2a x 2a x √2a
	Pb	2 a	$\bar{1}$	
		2 d		
	Cs	2 e	m	
		2 e'		
	Cl-I	2 e''	m	
		2 e'''		
	Cl-II	4 f	1	
	Cl-III	4 f'	1	

Table II

Coulomb coefficients of cubic perovskite structure ABX_3 shown in Fig.1. When these values are multipied by $(e^2/v)Z_\kappa Z_{\kappa'}$, ,they give the Coulomb contributions to the dynamical matrix.

$$q = \left(\frac{1}{2}\frac{1}{2}\zeta\right)$$

B - B

ζ	xx	yy	zz	xy	yz	zx
0.5	0	0	0	0	0	0
0.4	0.245	0.245	-0.490	0	0	0
0.3	0.897	0.897	-1.794	0	0	0
0.2	1.724	1.724	-3.448	0	0	0
0.1	2.410	2.410	-4.820	0	0	0
0	2.677	2.677	-5.354	0	0	0

B - X_{III}

ζ	xx	yy	zz	xy	yz	zx
0.5	0	0	0	0	0	0
0.4	0	0	0	0	0	1.062
0.3	0	0	0	0	0	1.738
0.2	0	0	0	0	0	1.764
0.1	0	0	0	0	0	1.103
0	0	0	0	0	0	0

B - A

ζ	xx	yy	zz	xy	yz	zx
0.5	0	0	0	0	0	0
0.4	0	0	0	3.124	0	0
0.3	0	0	0	6.023	0	0
0.2	0	0	0	8.430	0	0
0.1	0	0	0	10.047	0	0
0	0	0	0	10.620	0	0

A - X_I

ζ	xx	yy	zz	xy	yz	zx
0.5	0	0	0	14.461	0	0
0.4	0	0	0	14.698	0	0
0.3	0	0	0	15.331	0	0
0.2	0	0	0	16.134	0	0
0.1	0	0	0	16.801	0	0
0	0	0	0	17.060	0	0

B - X_I

ζ	xx	yy	zz	xy	yz	zx
0.5	0	0	0	0	0	0
0.4	4.959	4.959	-9.918	0	0	0
0.3	9.513	9.513	-19.026	0	0	0
0.2	13.234	13.234	-26.468	0	0	0
0.1	15.695	15.695	-31.390	0	0	0
0	16.559	16.559	-33.118	0	0	0

A - X_{III}

ζ	xx	yy	zz	xy	yz	zx
0.5	0	0	0	0	14.461	0
0.4	0	0	0	0	13.824	0
0.3	0	0	0	0	11.920	0
0.2	0	0	0	0	8.808	0
0.1	0	0	0	0	4.695	0
0	0	0	0	0	0	0

Figure Captions

Fig.1 (a) The unit cell of cubic perovskite structure ABX_3. (b) The reciprocal lattice of simple cubic structure.

Fig.2 The displacement patterns of the X ions in the triply degenerate R_{25} mode.

Fig.3 The displacement patterns of the X ions in (a) R_{25} and (b) M_3 modes. (c) The projection of the tetragonal structure in the z-plane which is stabilized by the condensation of the R_{25} mode or M_3 mode.

Fig.4 Temperature dependence of the Cl^{35} NQR frequency in $CsPbCl_3$, after Jensen.

Fig.5 The phase transition schemes of $CsPbCl_3$.

Fig.6 Temperature dependences of the superlattice Bragg reflections observed at the zone boundary points M, R and X along [110], [111] and [001] directions of the pseudo-cubic lattice, respectively. Three arrows indicate the phase transition points.

Fig.7 Temperature dependence of the specific heat of $CsPbCl_3$ measured by the a.c. calorimetry method. Three peaks correspond to the phase transition points.

Fig.8 Phonon dispersion curves of the acoustic branches along the symmetric directions at 80°C. The parts which are shown by the broken lines were not accurate because of the broadening of the spectra.

Fig.9 Temperature dependences of the quasi-elastic scatterings at M-point $(\frac{3}{2},\frac{1}{2},0)$.

Fig.10 Temperature dependences of the quasi-elastic scatterings at R-point$(\frac{3}{2},\frac{1}{2},\frac{1}{2})$.

Fig.11 The anisotropic distribution of the quasi-elastic scatterings around the M-point$(\frac{3}{2},\frac{1}{2},0)$ in Phase I. The large solid and open triangles at the origin represent the resolution functions in the q-space along the directions $[\frac{1}{2}\ \frac{1}{2}\ \zeta]$ and $[\frac{1}{2}+\zeta,\frac{1}{2}+\frac{\zeta}{3},0]$, respectively. The distance between the M-point and R-point is 0.566 A^{-1} at 80°C.

Fig.12 Temperature dependences of the quasi-elastic scattering (open circles) and the superlattice Bragg reflection (solid circles) at the M-point$(\frac{3}{2},\frac{1}{2},0)$.

Fig.13 Comparison between the observed dynamical structure factors(open circles) at 80°C and the calculated ones (solid circles) for the M_3 mode at various M-points$(\frac{1}{2},\frac{1}{2},0)$.

Fig.14 Comparison between the observed dynamical structure factors at 55°C(open circles) and the calculated ones (solid circles) for the R_{25} mode at various R-points$(\frac{1}{2},\frac{1}{2},\frac{1}{2})$.

Fig.15 Temperature dependences of the quasi-elastic scattering (open circles) and the superlattice Bragg reflection (solid circles) at R-point$(\frac{3}{2},\frac{3}{2},\frac{5}{2})$. The discrete increase in the quasi-elastic scattering corresponds to the cubic-to-tetragonal transition point.

Fig.16 Temperature dependences of the quasi-elastic scattering (open circles) and the superlattice Bragg reflection (solid circles) at X-point$(1,1,\frac{3}{2})$. The remaining temperature independent intensity above 47°C is due to the incoherent scattering, which means that there is

no quasi-elastic scattering above 47°C at the X-point in contrast with the R-point(Fig.15).

Fig.17 Relation between reciprocal lattice of the tetragonal structure (q_x^t, q_y^t and q_z^t) stabilized by the condensation of the M_3 mode(drawn with the thick lines) and that of the cubic structure (q_x^c, q_y^c and q_z^c)(drawn with the thin lines). The symbols in parentheses are referred to the tetragonal structure and those out of parentheses are referred to the cubic one.

Fig.18 Comparison between the observed dynamical structure factors (open circles) at 45°C and the calculated ones (solid circles) for the Z_5^x mode at various X-points $(0,0,\frac{1}{2})$.

Fig.19 Comparison between the observed dynamical structure factors (open circles) at 45°C and the calculated ones (solid circles) for the Z_5^x mode at various R-points $(\frac{1}{2}\ \frac{1}{2}\ \frac{1}{2})$.

Fig.20 The crystal structure at Phase III stabilized by the condensation of the Z_5^x.

Fig.21 The crystal structure at Phase IV stabilized by the condensation of the Z_5^y mode.

Fig.22 A schematic diagram of the free energy at each phase.

Fig.23 The stable region of Phase III and Phase IV with respect to the coefficients D' and E'. The arrows represent the trace of the temperature dependence of the system.

Fig.24 A schematic diagram of the temperature dependences of the order parameters.

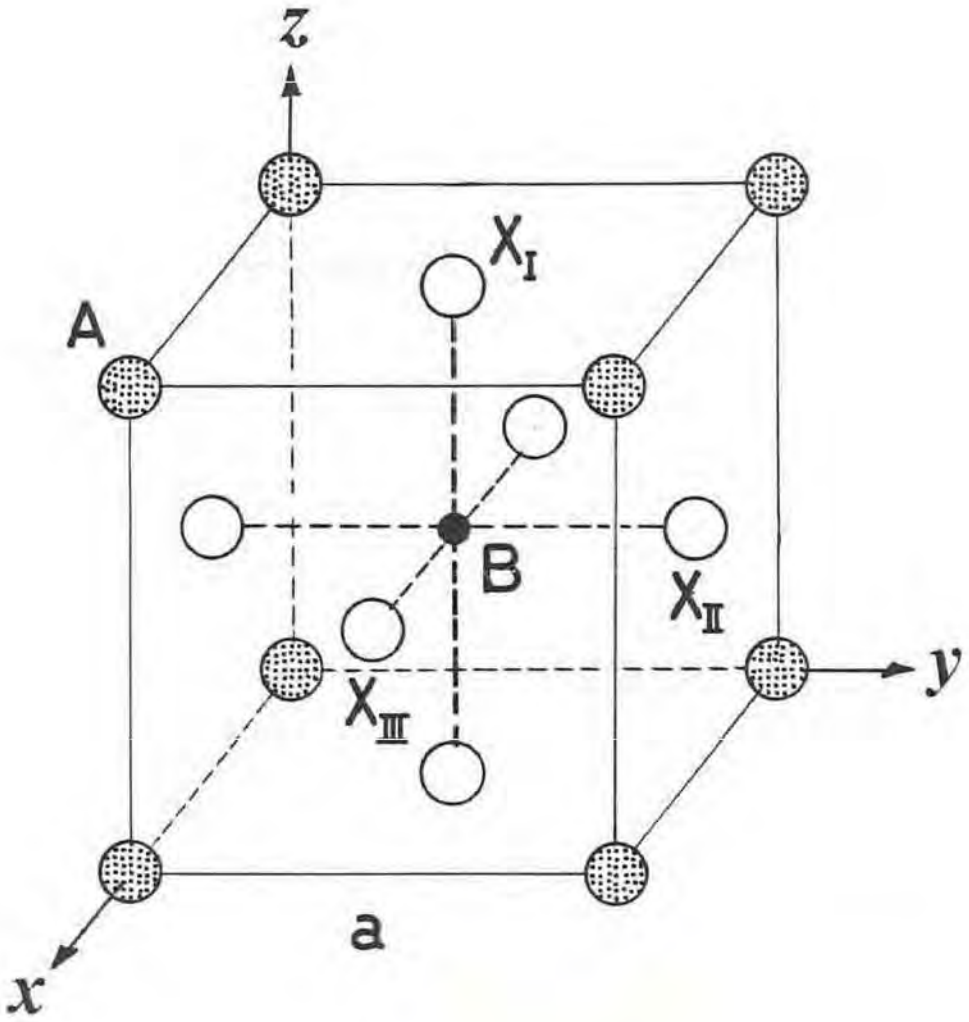

(a)

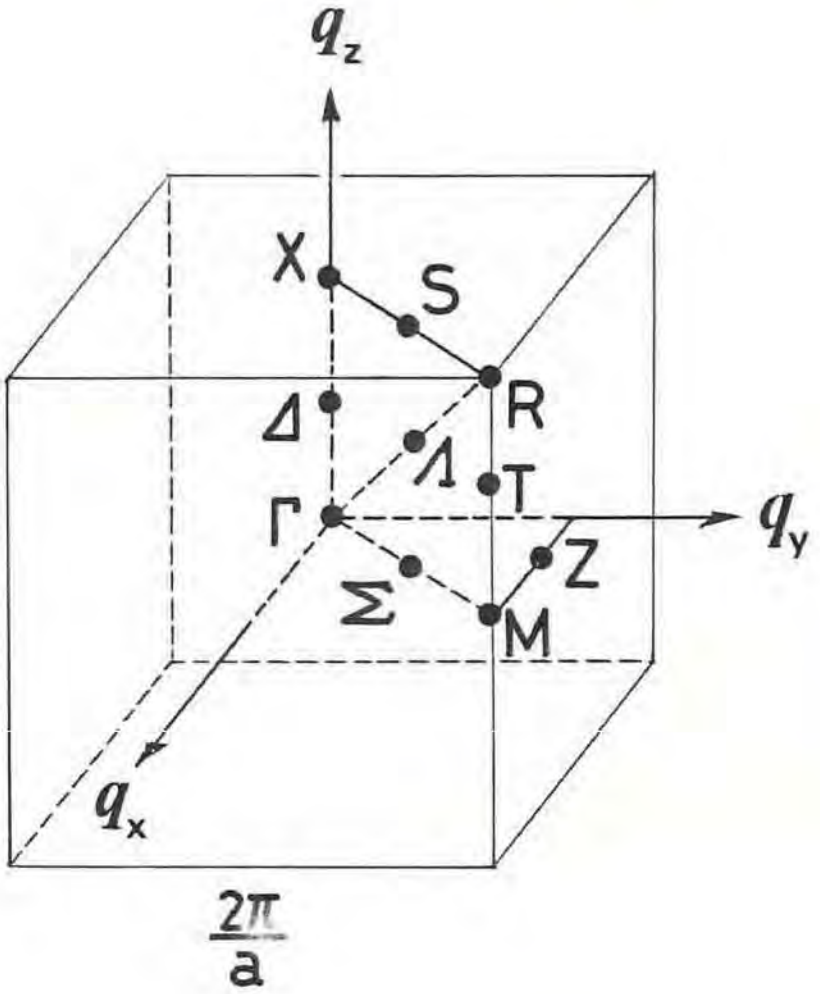

(b)

FIG.1

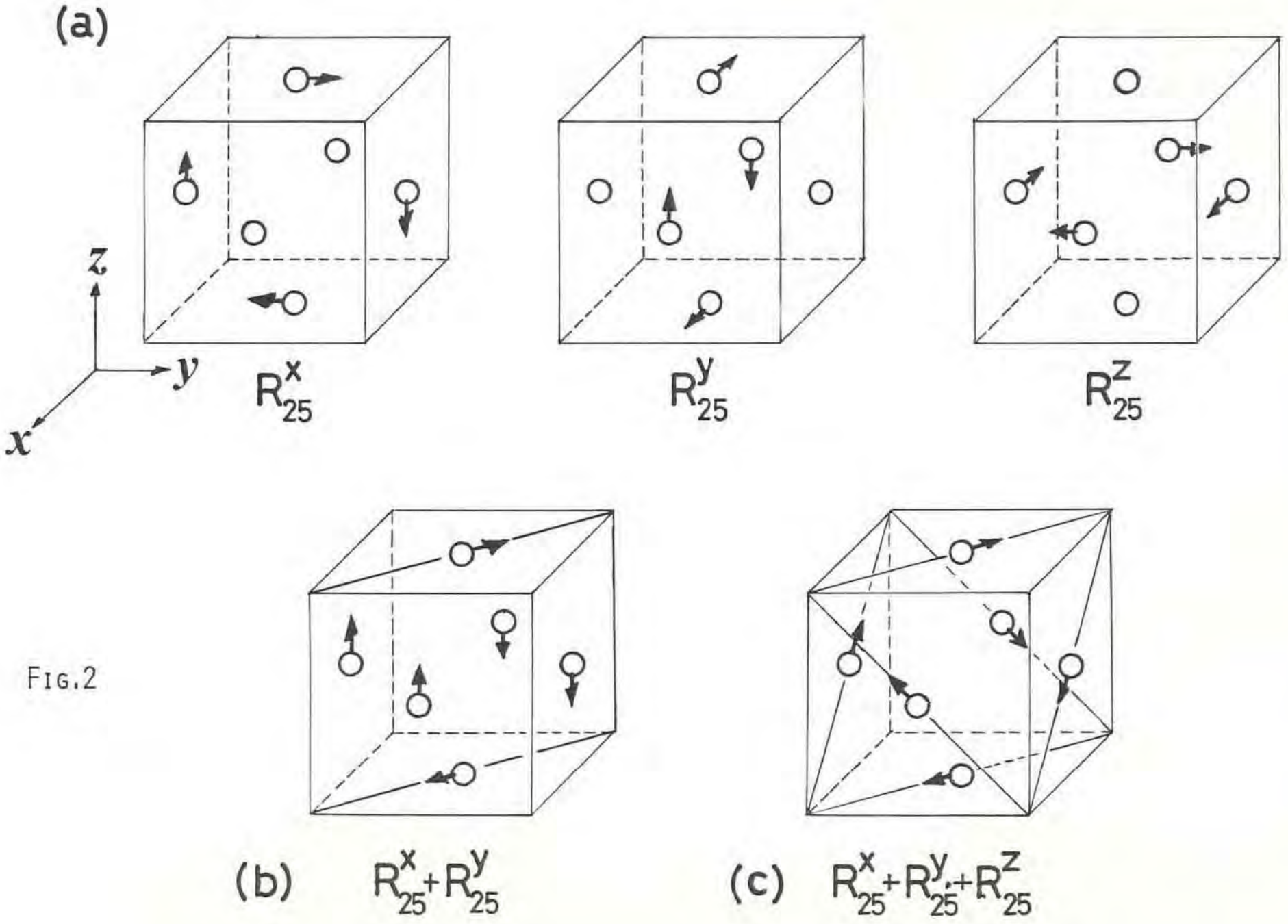

FIG.2

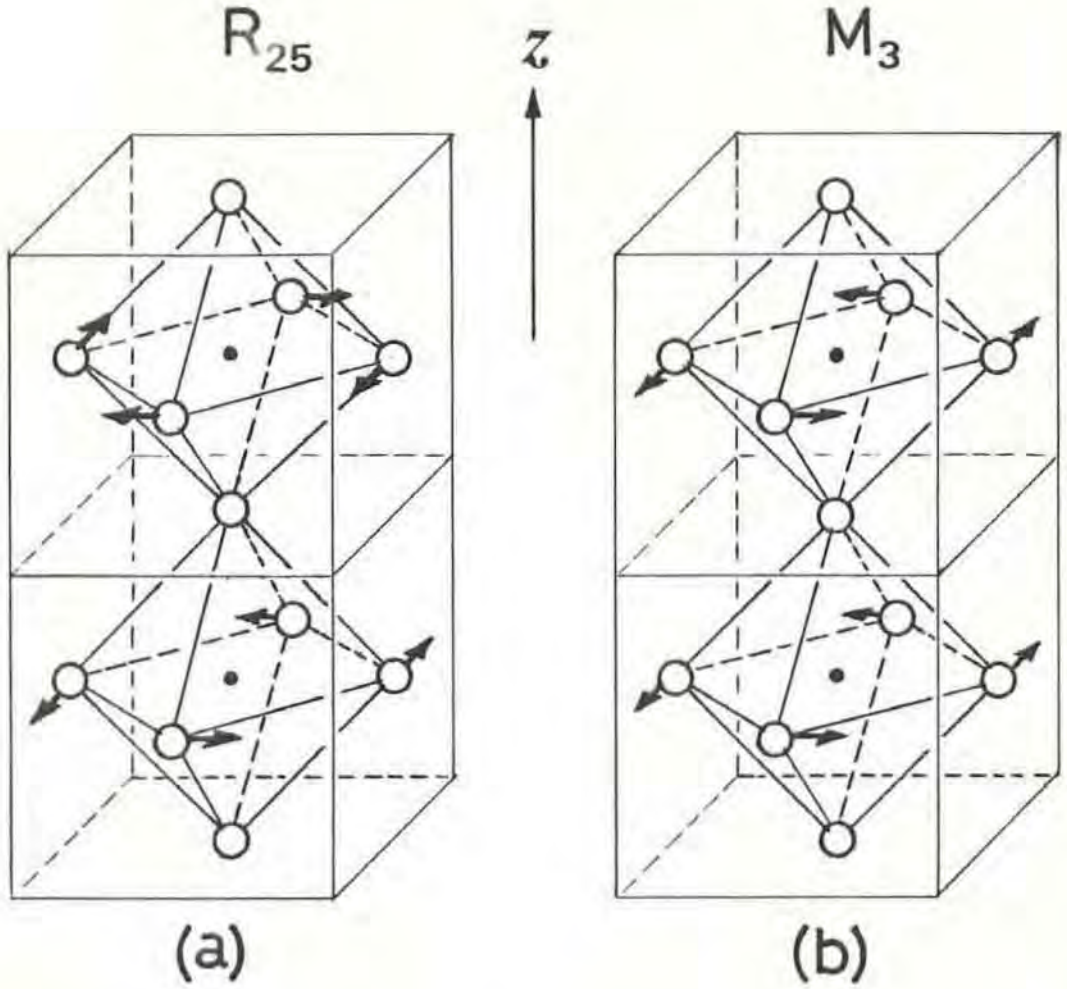

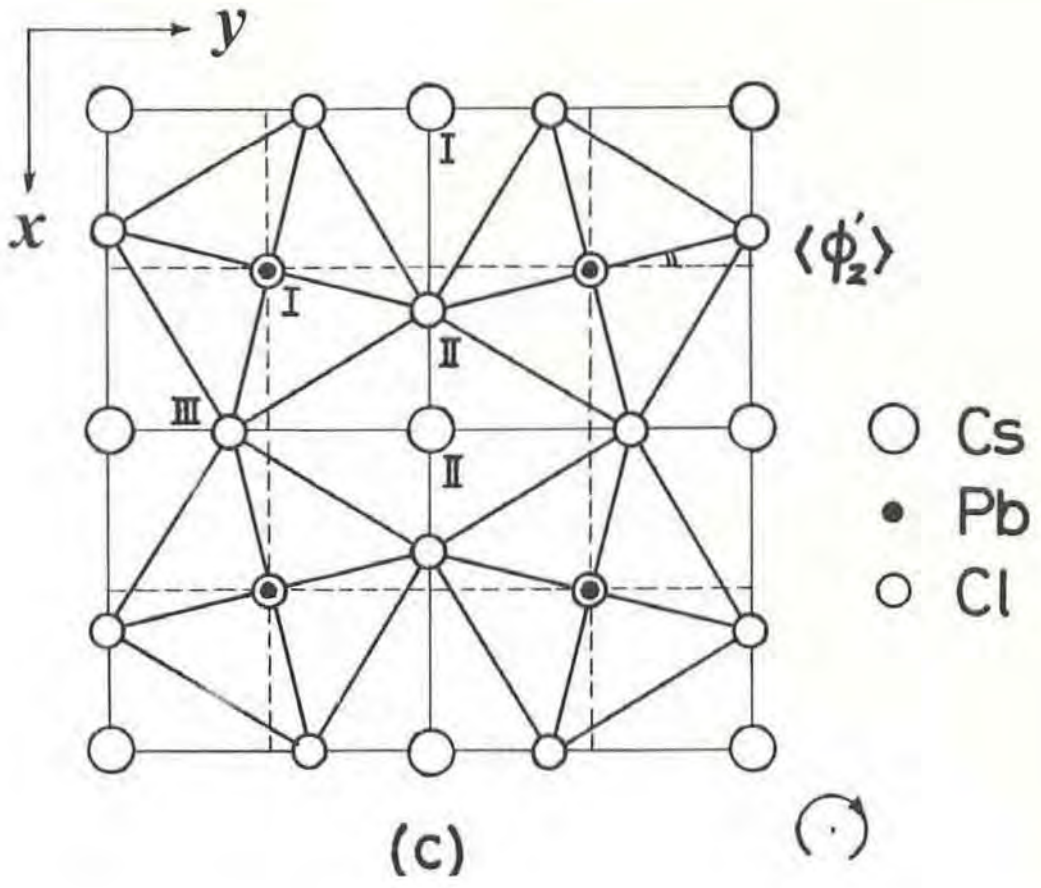

FIG.3

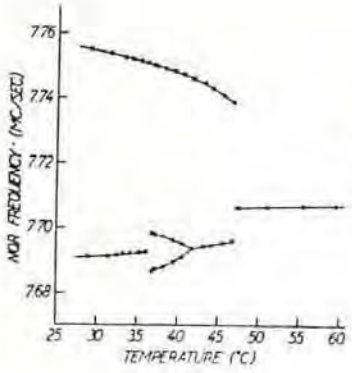

The ^{35}Cl NQR frequency in $CsPbCl_3$ as a function of temperature. The linewidth is about 1.5 kc/sec.

FIG.4

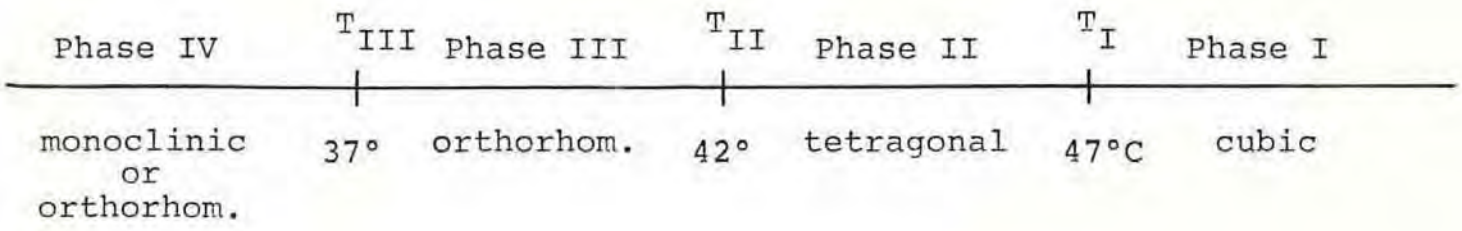

FIG.5

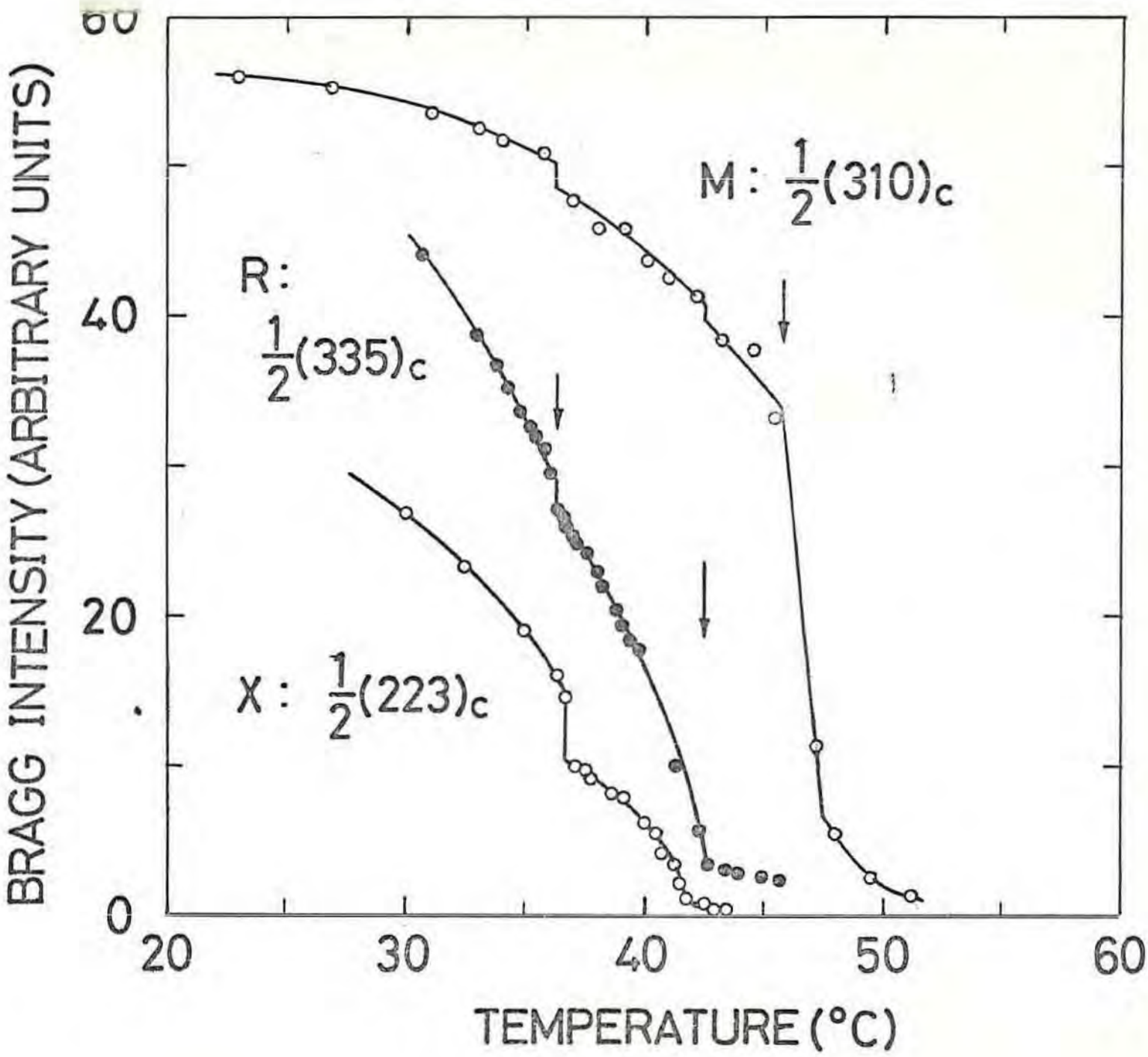
BRAGG INTENSITY (ARBITRARY UNITS)
0
20
40
60
20
30
40
50
60
TEMPERATURE (°C)
M: $\frac{1}{2}(310)_c$
R: $\frac{1}{2}(335)_c$
X: $\frac{1}{2}(223)_c$

FIG.6

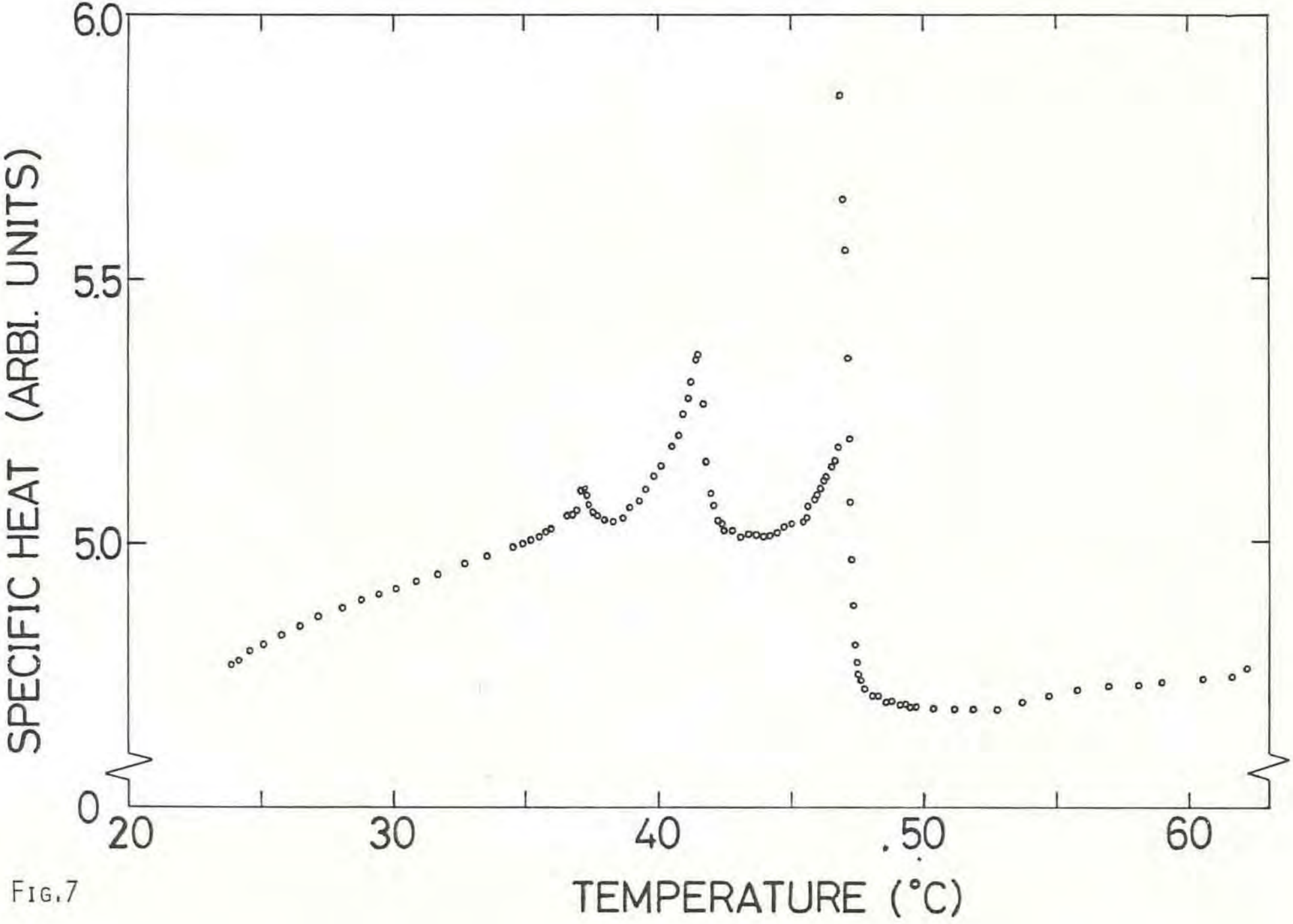
6.0
5.5
5.0
0
20
30
40
50
60
SPECIFIC HEAT (ARBI. UNITS)
TEMPERATURE (°C)

FIG. 7

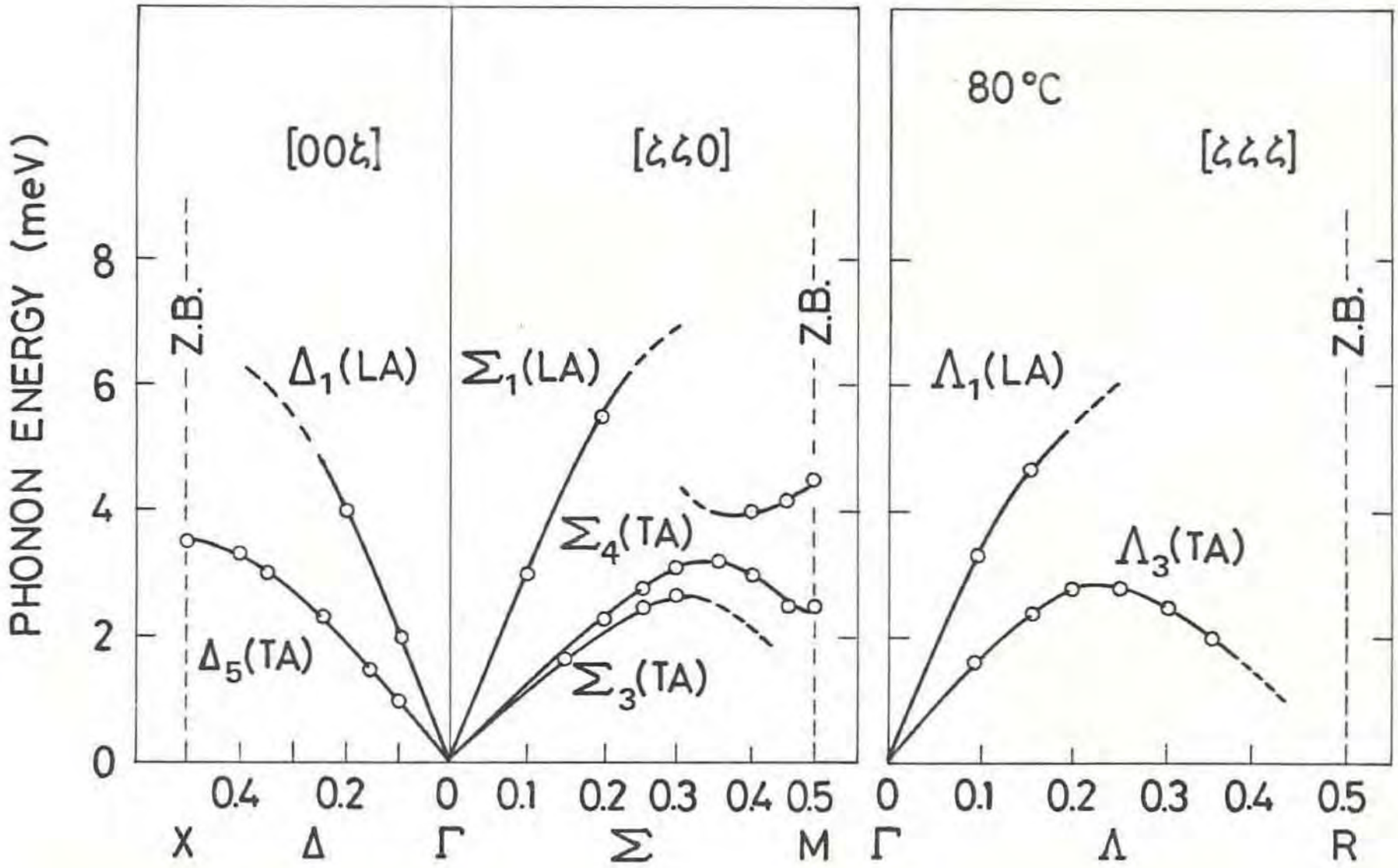
PHONON ENERGY (meV)
80 °C
[00ζ]
[ζζ0]
[ζζζ]
Z.B.
Z.B.
Z.B.
Δ1(LA)
Σ1(LA)
Λ1(LA)
Σ4(TA)
Λ3(TA)
Δ5(TA)
Σ3(TA)
0
2
4
6
8
0.4
0.2
0
0.1
0.2
0.3
0.4
0.5
X
Δ
Γ
Σ
M
Γ
Λ
R

FIG.8

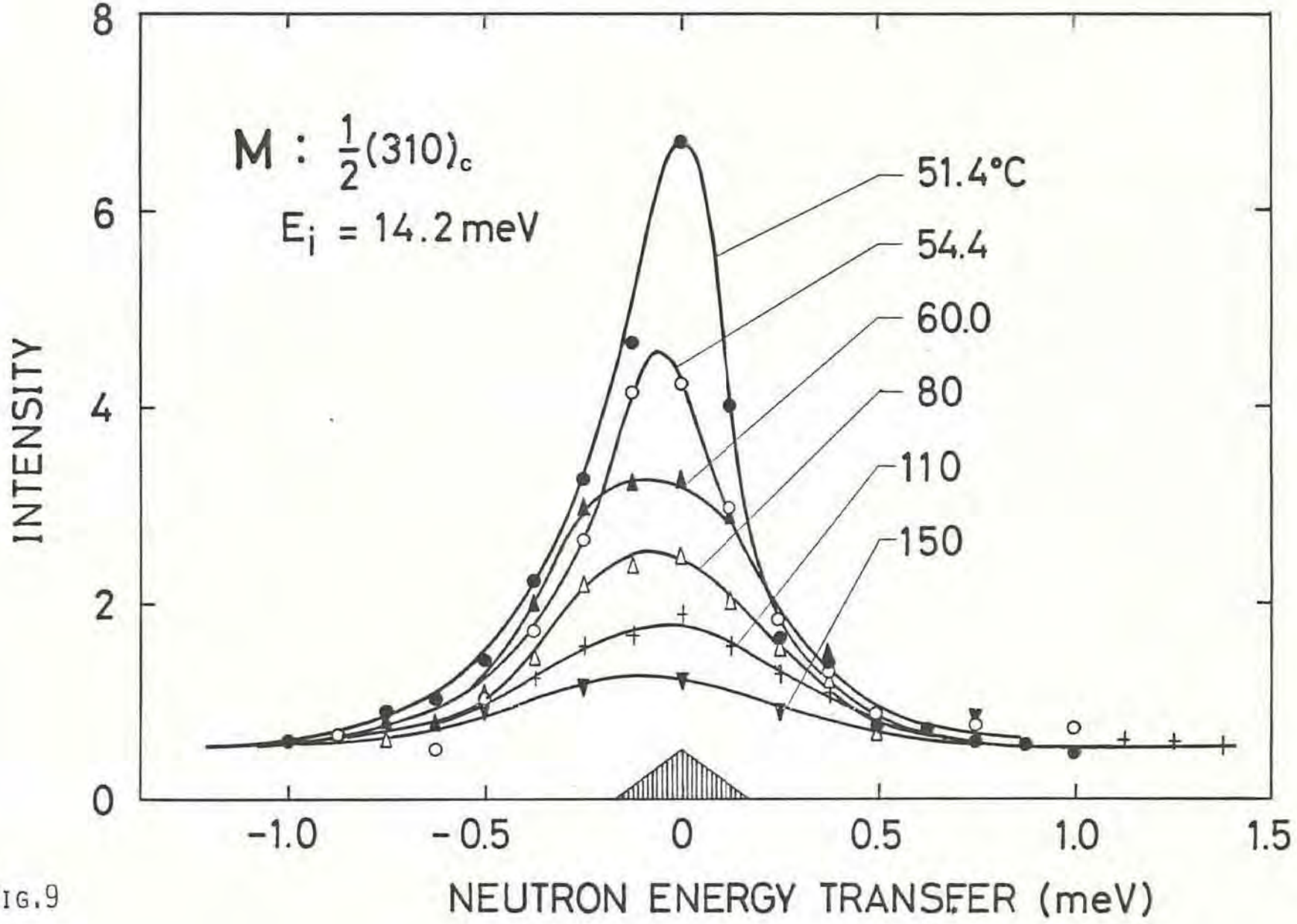
M : $\frac{1}{2}(310)_c$
E_i = 14.2 meV
51.4°C
54.4
60.0
80
110
150
INTENSITY
NEUTRON ENERGY TRANSFER (meV)
0
2
4
6
8
-1.0
-0.5
0
0.5
1.0
1.5

FIG.9

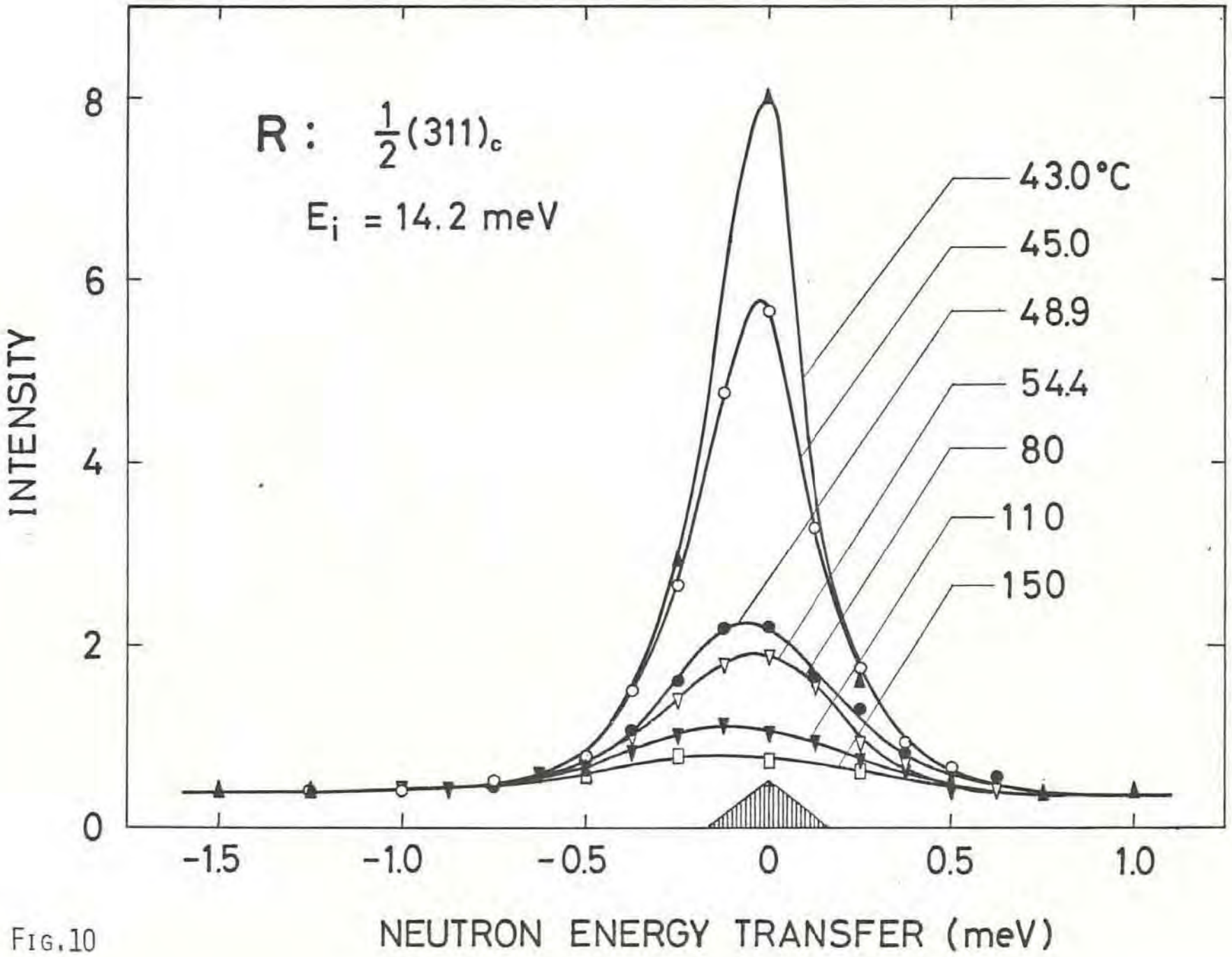
R : $\frac{1}{2}(311)_c$
E_i = 14.2 meV
43.0°C
45.0
48.9
54.4
80
110
150
INTENSITY
0
2
4
6
8
-1.5
-1.0
-0.5
0
0.5
1.0
NEUTRON ENERGY TRANSFER (meV)

FIG.10

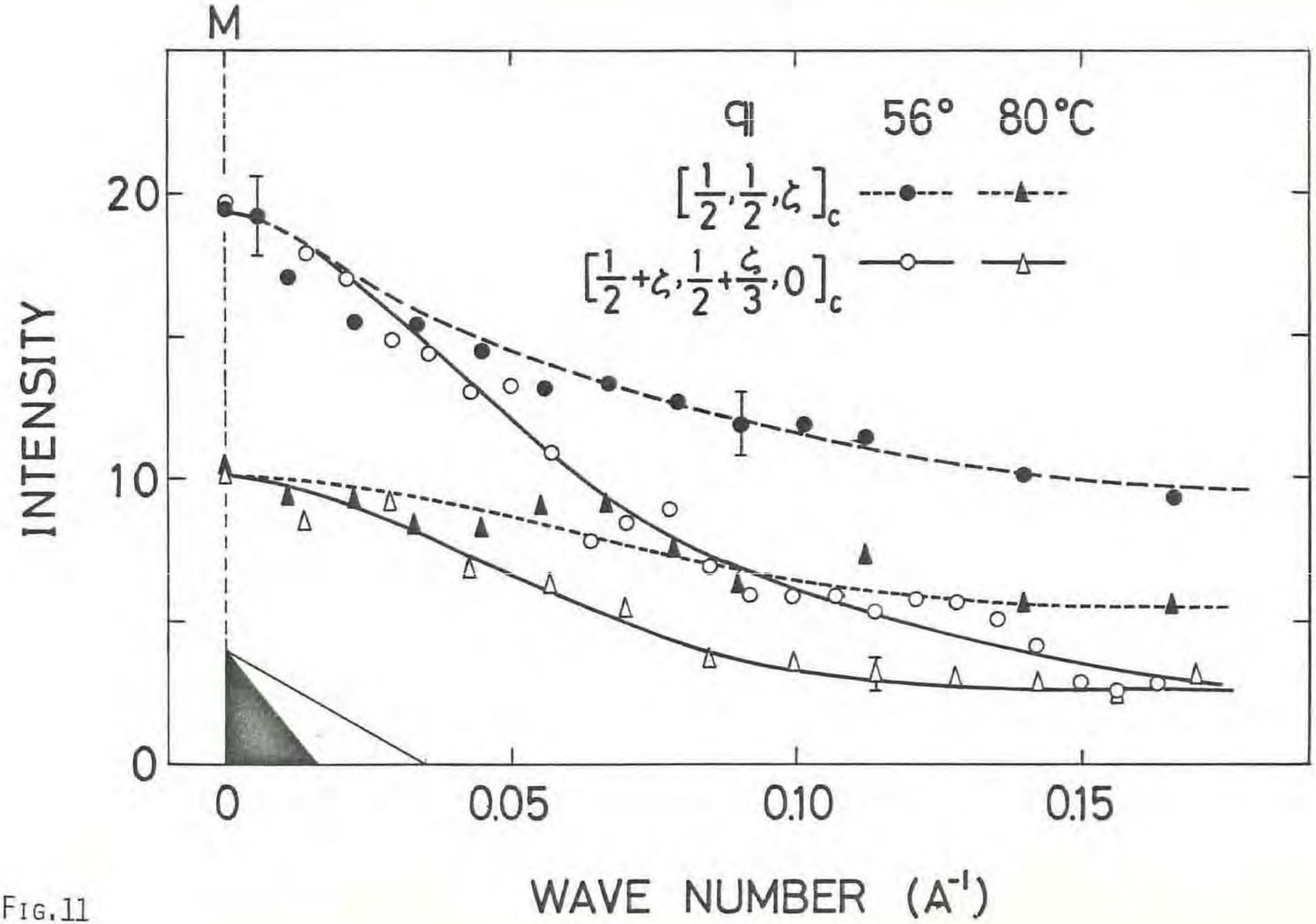
M
q∥
56°
80°C
$[\frac{1}{2},\frac{1}{2},\zeta]_c$
$[\frac{1}{2}+\zeta,\frac{1}{2}+\frac{\zeta}{3},0]_c$
INTENSITY
20
10
0
0
0.05
0.10
0.15
WAVE NUMBER (A^{-1})

FIG. 11

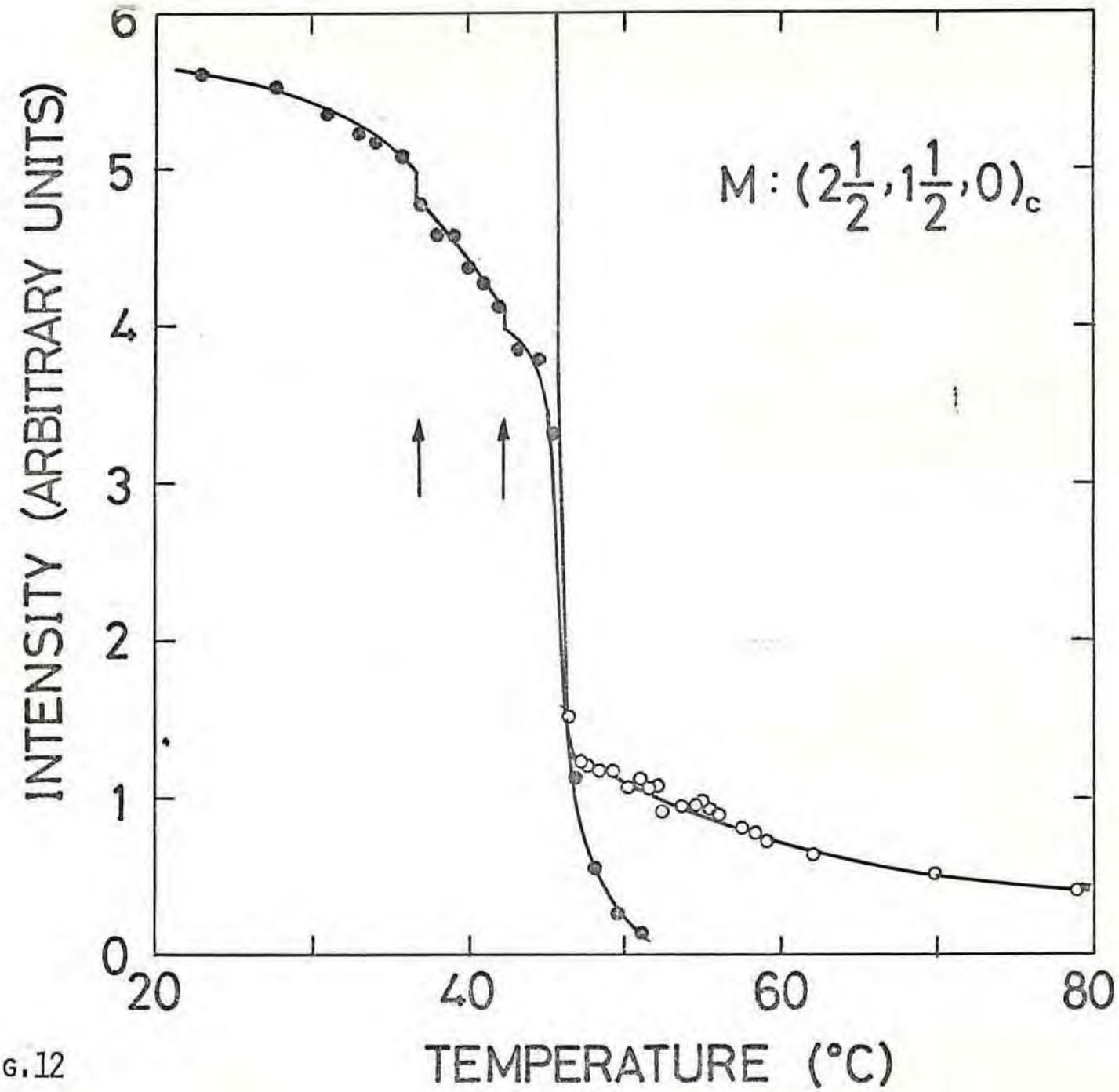
INTENSITY (ARBITRARY UNITS)
0
1
2
3
4
5
6
20
40
60
80
TEMPERATURE (°C)
M : $(2\frac{1}{2}, 1\frac{1}{2}, 0)_c$

FIG. 12

|Fd(M)| (ARBI. UNITS)
0
1
2
3
4
5
M3
80°C
obs.
cal.
(1/2 1/2 0)
(1 1/2 1/2 0)
(1 1/2 1 1/2 0)
(2 1/2 1/2 0)
(2 1/2 1 1/2 0)
(2 1/2 2 1/2 0)
(3 1/2 1/2 0)
(3 1/2 1 1/2 0)

FIG. 13

|Fd(R)| (ARBI. UNITS)
0
1
2
3
4
5
R25
55°C
obs.
cal.
(1/2 1/2 1/2)
(1/2 1/2 1 1/2)
(1 1/2 1 1/2 1/2)
(1 1/2 1 1/2 1 1/2)
(1/2 1/2 2 1/2)
(1 1/2 1 1/2 2 1/2)
(2 1/2 2 1/2 1/2)
(1/2 1/2 3 1/2)
(2 1/2 2 1/2 1 1/2)

FIG. 14

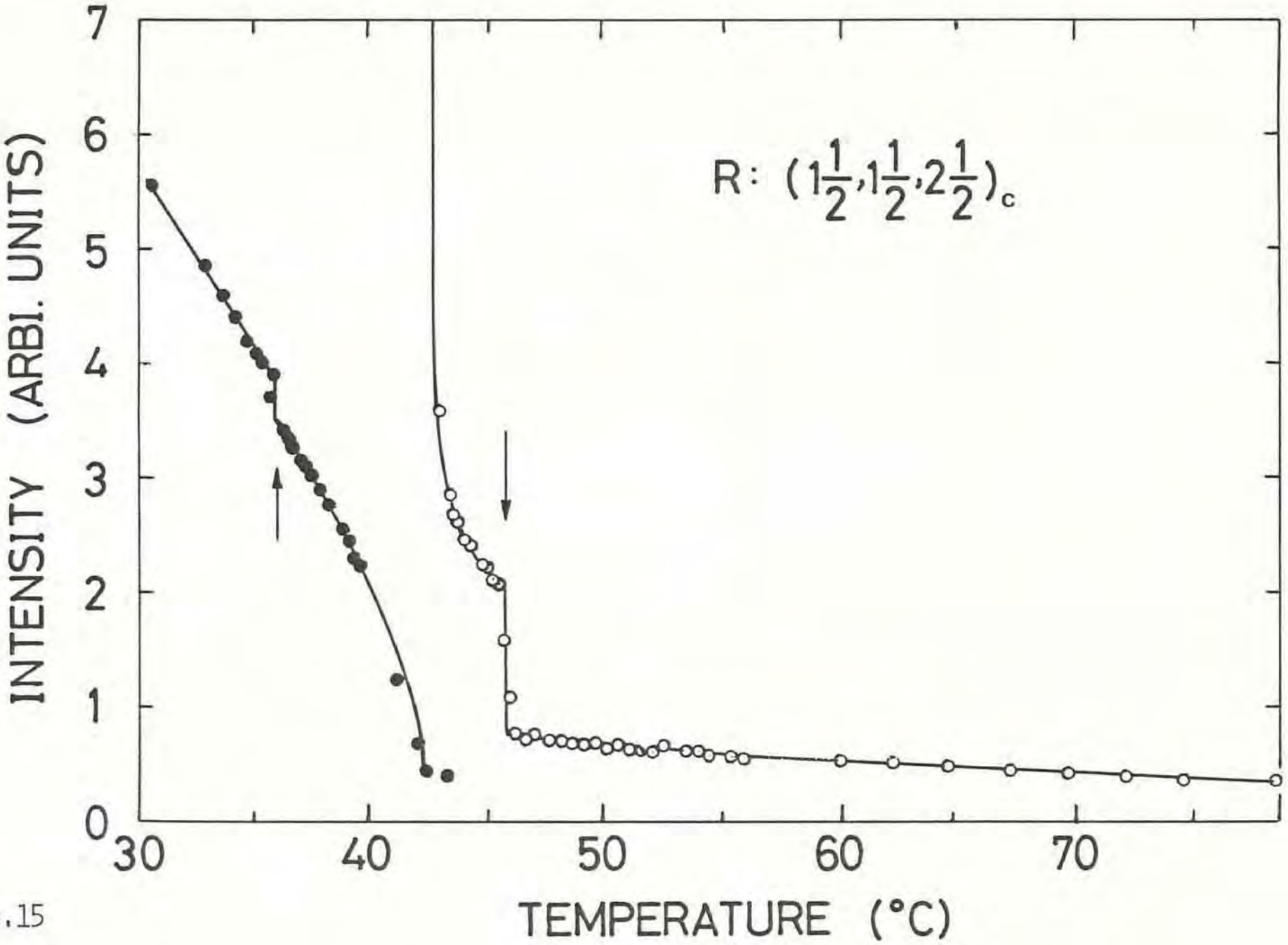
INTENSITY (ARBI. UNITS)
TEMPERATURE (°C)
R: $(1\frac{1}{2}, 1\frac{1}{2}, 2\frac{1}{2})_c$
0
1
2
3
4
5
6
7
30
40
50
60
70

FIG. 15

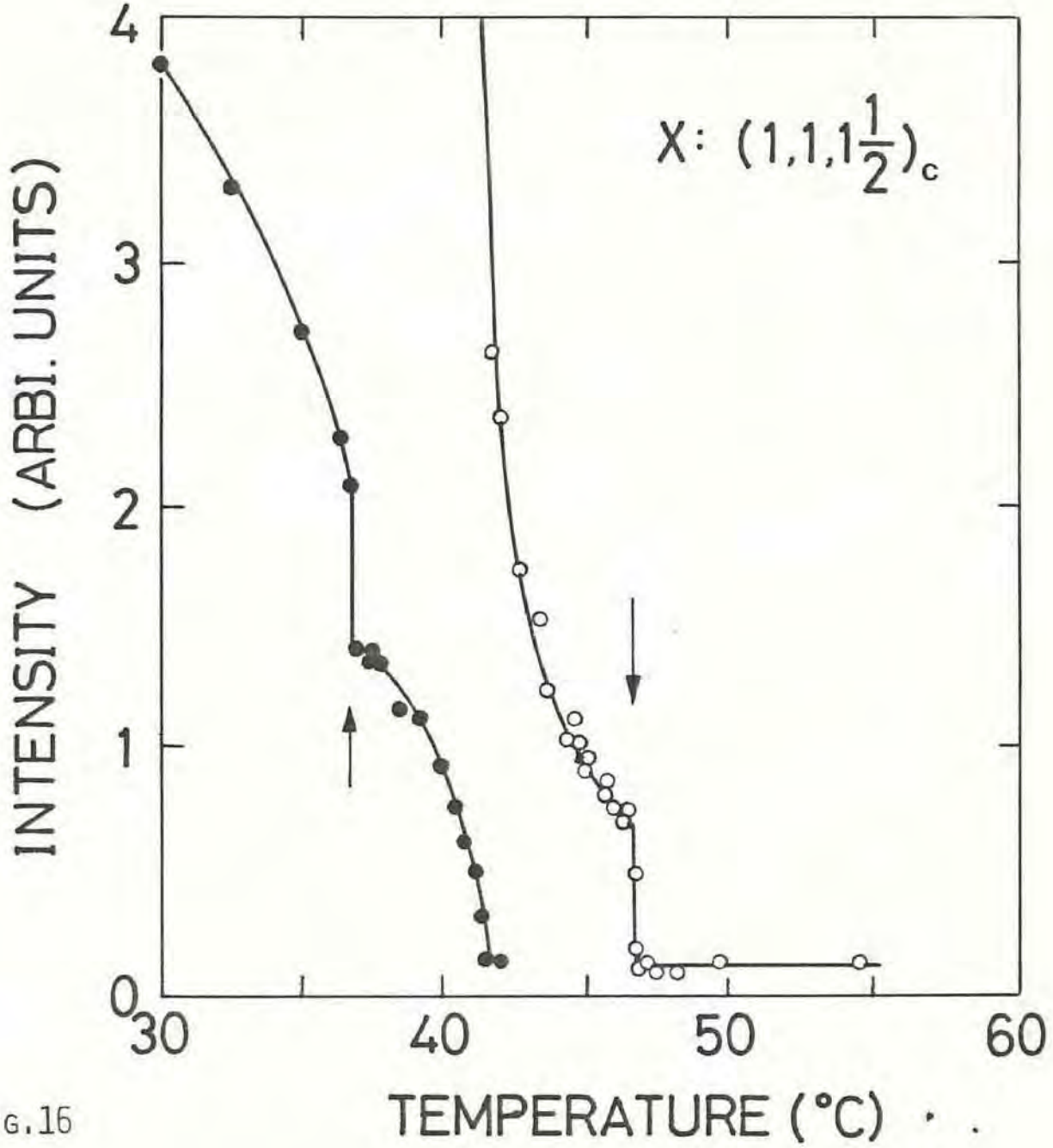
INTENSITY (ARBI. UNITS)
TEMPERATURE (°C)
X: $(1,1,1\frac{1}{2})_c$
0
1
2
3
4
30
40
50
60

FIG.16

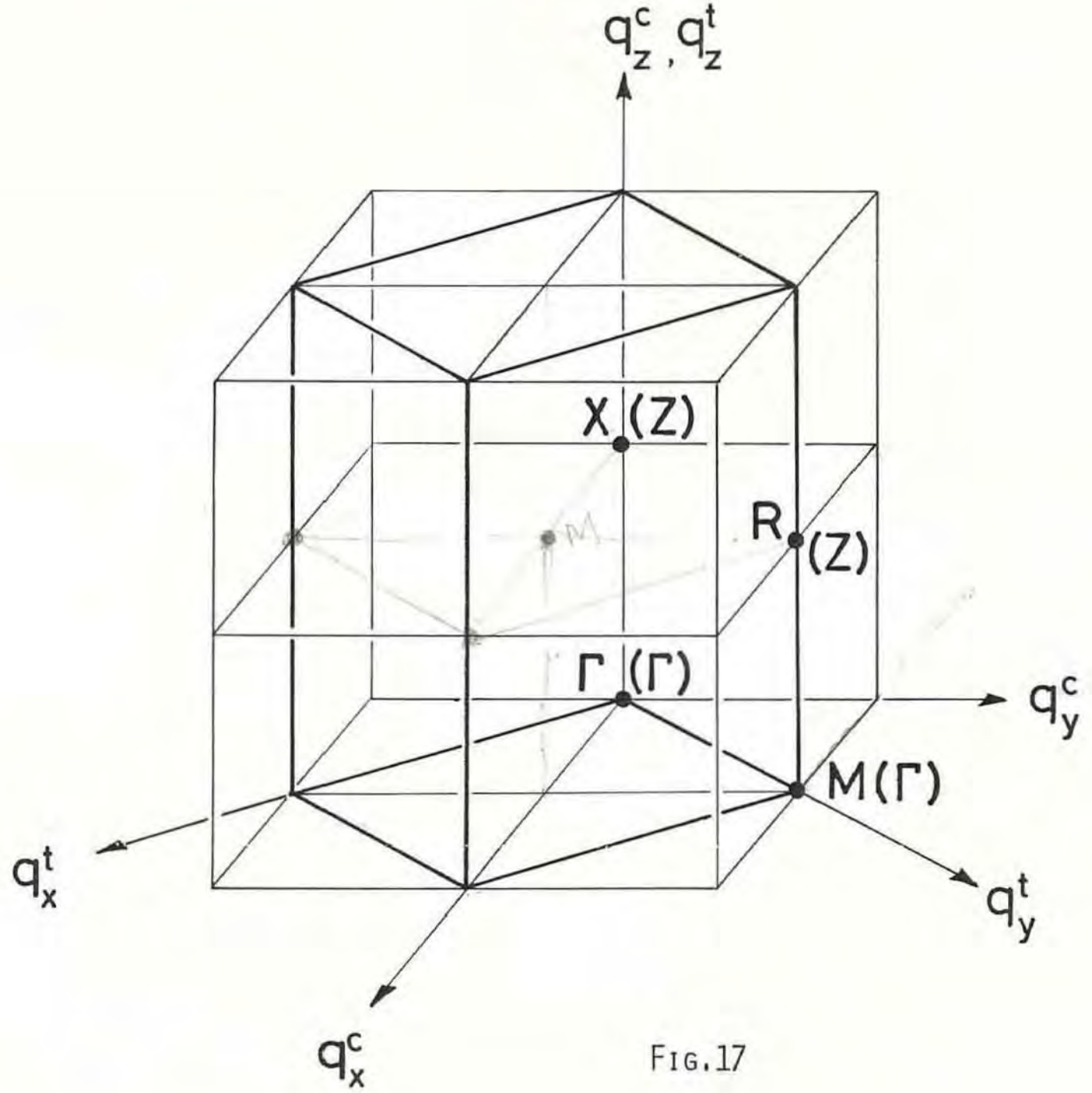

FIG. 17

Z5 R-POINT 45°C
obs.
cal.
|Fd(X)| (ARBI. UNITS)
(1/2 1/2 1/2)
(1/2 1/2 1 1/2)
(1 1/2 1 1/2 1/2)
(1 1/2 1 1/2 1 1/2)
(1/2 1/2 2 1/2)
(1 1/2 1 1/2 2 1/2)
(2 1/2 2 1/2 1/2)
(1/2 1/2 3 1/2)
(2 1/2 2 1/2 1 1/2)

Fig. 19

Z5 X-POINT 45 °C
obs.
cal.
|Fd(X)| (ARBI. UNITS)
(0 0 1 1/2)
(1 1 1/2)
(1 1 1 1/2)
(0 0 2 1/2)
(1 1 2 1/2)
(2 2 1/2)
(2 2 1 1/2)
(0 0 3 1/2)
(1 1 3 1/2)
(2 2 2 1/2)

Fig. 18

D_{2h}^{17} – Cmcm

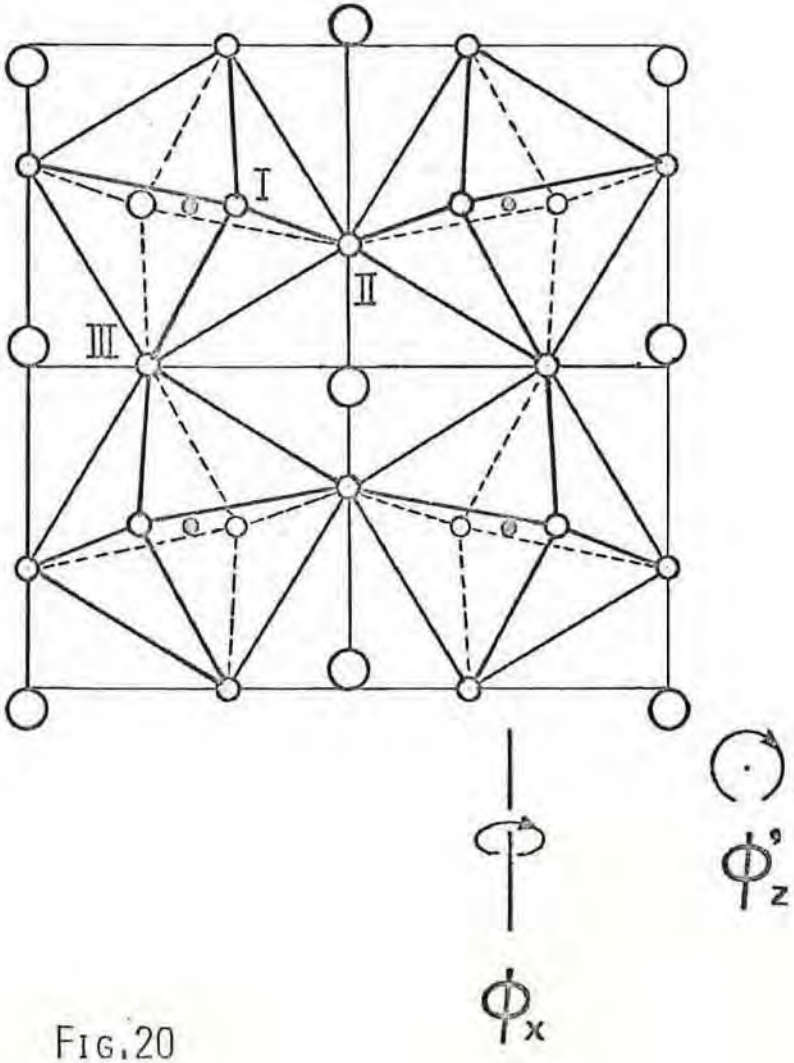

FIG.20

C_{2h}^{2} – $P2_1/m$, 7

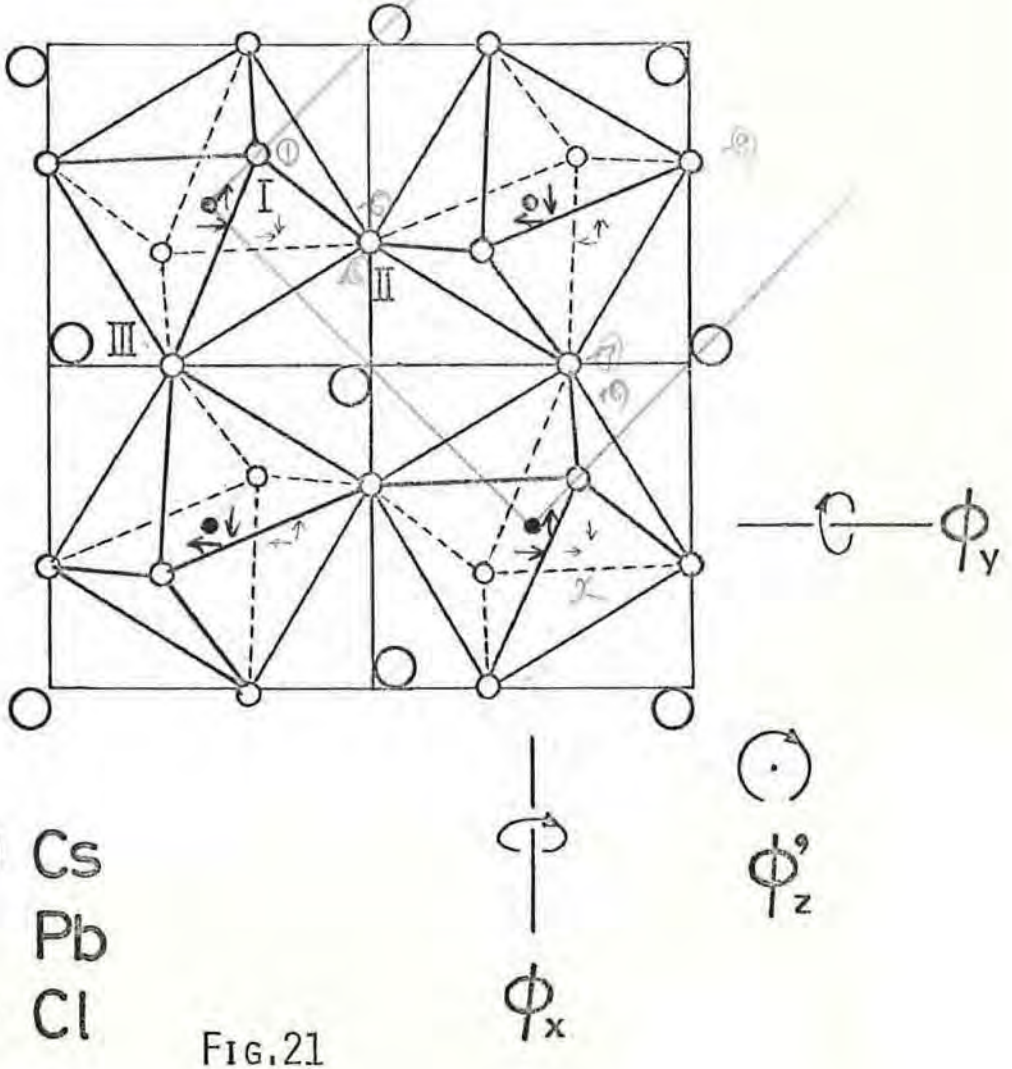

○ Cs
• Pb
○ Cl

FIG.21

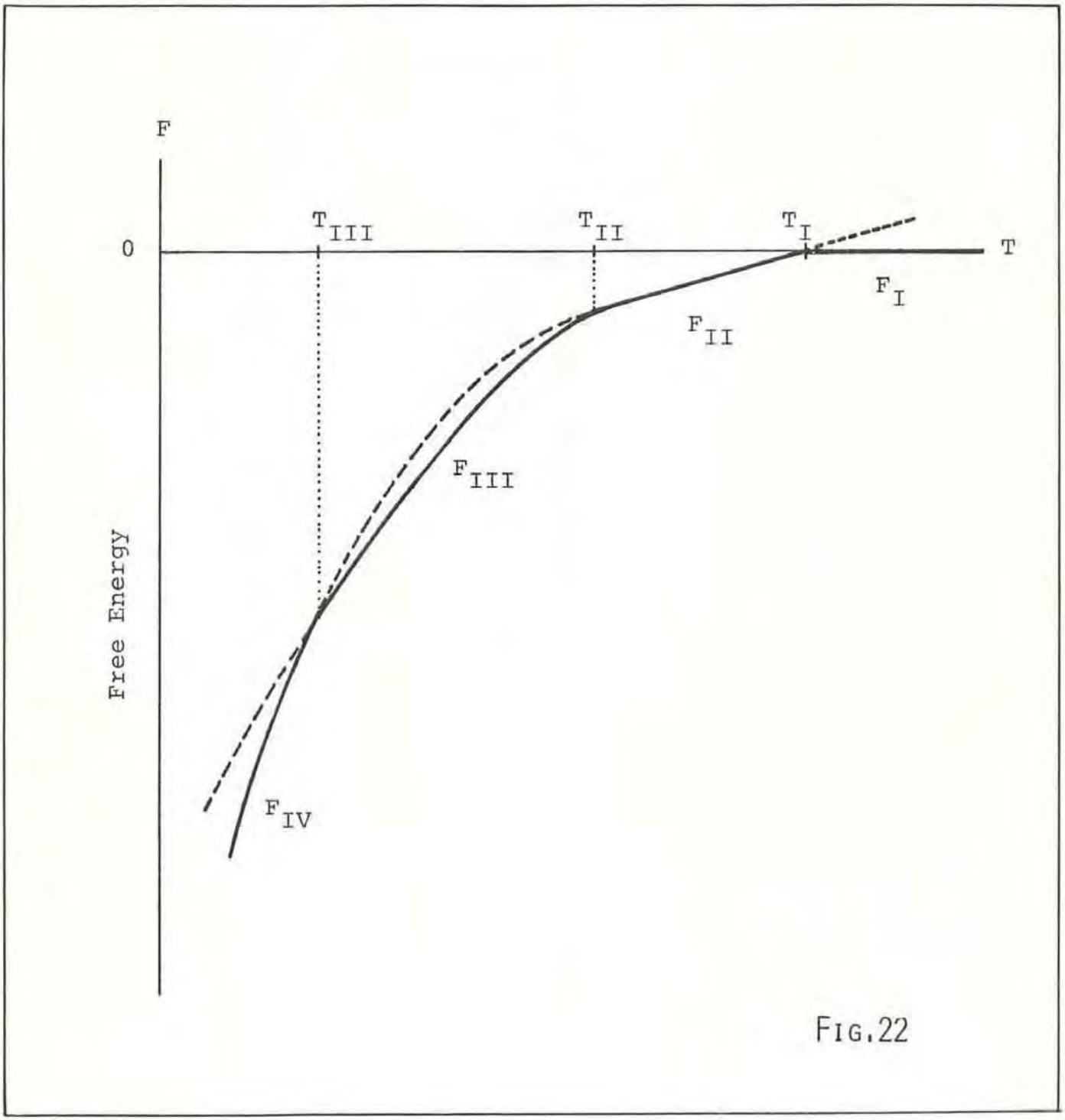

FIG.22

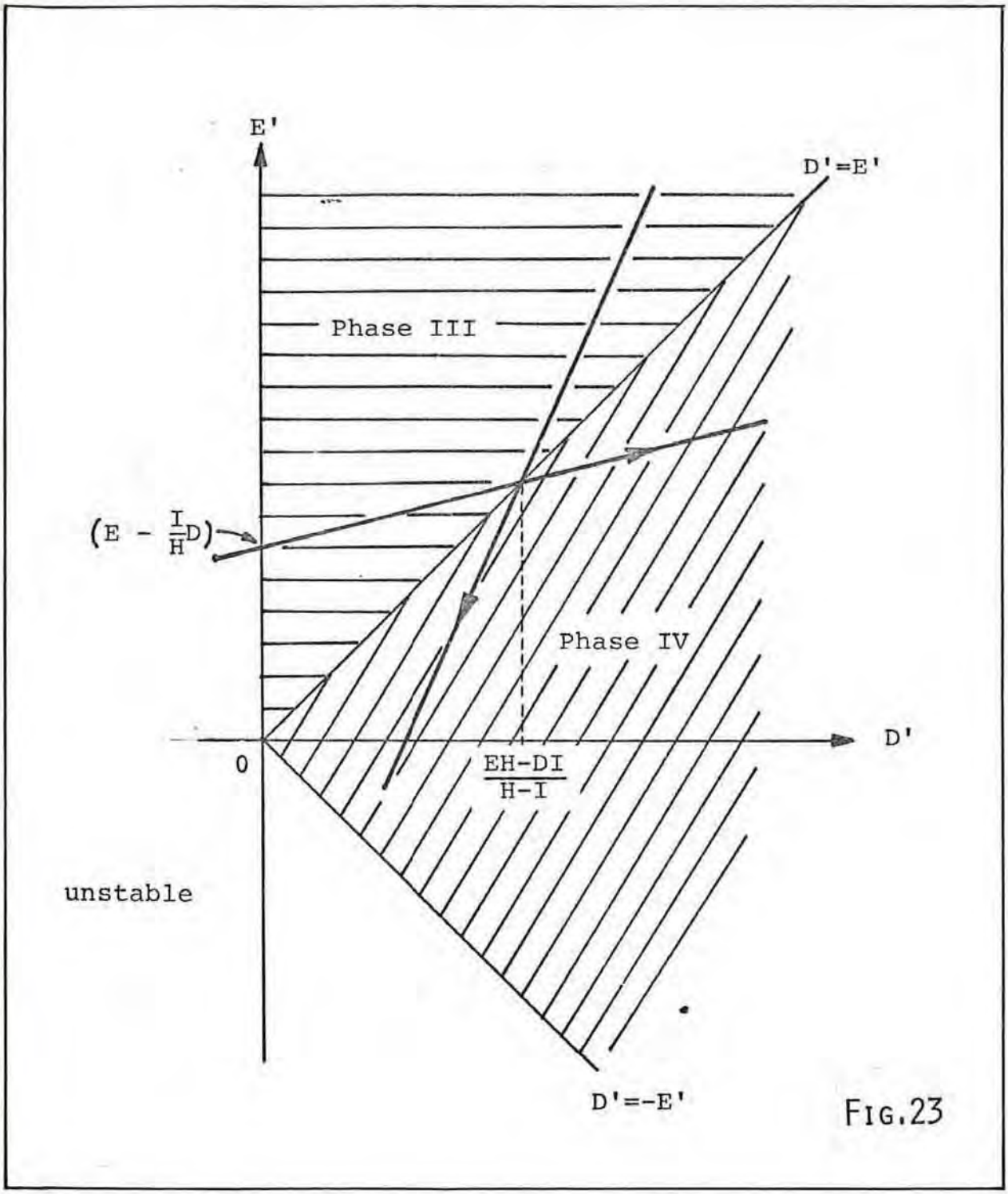

FIG.23

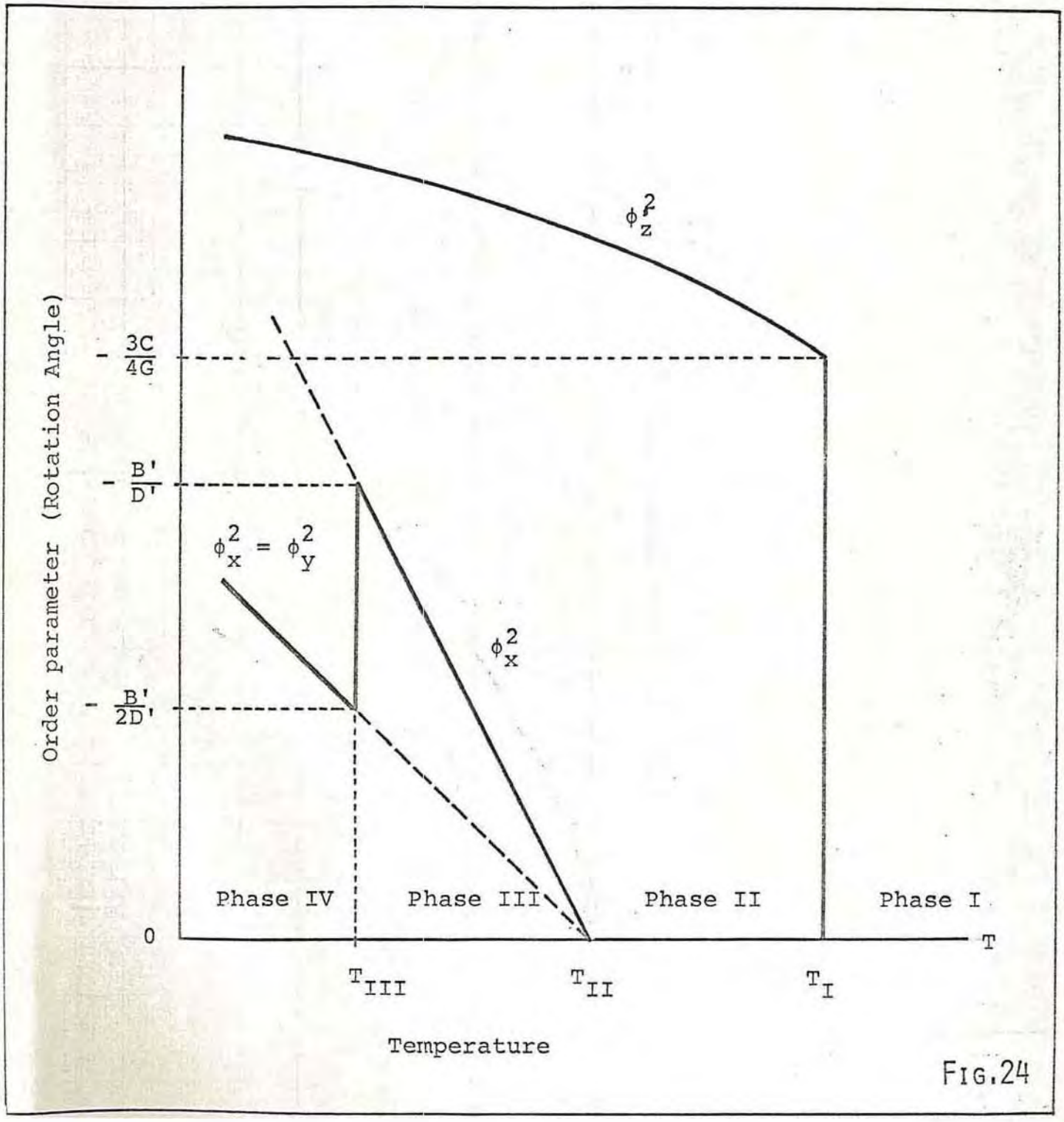
Order parameter (Rotation Angle)
$-\frac{3C}{4G}$
$-\frac{B'}{D'}$
$-\frac{B'}{2D'}$
ϕ_z^2
$\phi_x^2 = \phi_y^2$
ϕ_x^2
Phase IV
Phase III
Phase II
Phase I
0
T
T_{III}
T_{II}
T_I
Temperature

FIG.24